

# NASA TECHNICAL NOTE



NASA TN D-3800

NASA TN D-3800

GPO PRICE \$ \_\_\_\_\_

CFSTI PRICE(S) \$ \$2.50

Hard copy (HC) \_\_\_\_\_

Microfiche (MF) \$1.30

# 853 July 65

FACILITY FORM 802

<u>N67-15665</u>	
(ACCESSION NUMBER)	(THRU)
<u>60</u>	<u>1</u>
(PAGES)	(CODE)
(NASA CR OR TMX OR AD NUMBER)	<u>12</u> <del>_____</del>
	(CATEGORY)

## EXPERIMENTAL FLOW FIELD AND HEAT-TRANSFER INVESTIGATION OF SEVERAL TENSION SHELL CONFIGURATIONS AT A MACH NUMBER OF 8

*by Robert A. Jones, Dennis M. Bushnell, and James L. Hunt*

*Langley Research Center*

*Langley Station, Hampton, Va.*

EXPERIMENTAL FLOW FIELD AND HEAT-TRANSFER INVESTIGATION  
OF SEVERAL TENSION SHELL CONFIGURATIONS

AT A MACH NUMBER OF 8

By Robert A. Jones, Dennis M. Bushnell,  
and James L. Hunt

Langley Research Center  
Langley Station, Hampton, Va.

NATIONAL AERONAUTICS AND SPACE ADMINISTRATION

---

For sale by the Clearinghouse for Federal Scientific and Technical Information  
Springfield, Virginia 22151 - Price \$2.50

# EXPERIMENTAL FLOW FIELD AND HEAT-TRANSFER INVESTIGATION

## OF SEVERAL TENSION SHELL CONFIGURATIONS

### AT A MACH NUMBER OF 8

By Robert A. Jones, Dennis M. Bushnell,  
and James L. Hunt  
Langley Research Center

#### SUMMARY

An investigation was conducted at a Mach number of 8 to determine the flow field and pressure and heat-transfer distributions about several bell-shaped configurations called tension shells. This shape provides a possible minimum-weight entry vehicle structure since the shell can be designed as a tension member. Schlieren data were obtained over a range of free-stream Reynolds numbers based on model base diameter from  $0.1 \times 10^6$  to  $1.5 \times 10^6$  and angles of attack from  $0^\circ$  to  $31^\circ$ . These data indicated that certain of the shapes have unsteady flow fields with extensive regions of separated flow. The extent of separation and type of flow field were found to be functions of wall-to-total-temperature ratio, Reynolds number, nose bluntness, and base corner radius. Extensive separation can occur on the concave portion of some bodies, the result being that the effective shape is similar to a blunted cone. Certain other of the shapes had very little separation and a multiple-shock flow pattern was observed. Near the nose the shock lies close to the body but farther downstream a nearly normal shock is formed which results in very high pressures on the flare and correspondingly large drag coefficients.

Heat-transfer and pressure distributions were obtained at Reynolds numbers based on free-stream conditions and on model base diameter of  $0.2 \times 10^6$  and  $0.5 \times 10^6$ , respectively, for a configuration which seemed to have a more stable flow field and higher drag.

A few tests were made in a small facility which used  $\text{CF}_4$  (tetrafluoromethane) as the test gas in order to study the effect of normal shock density ratio on shock shape. The position of the nearly normal shock was found to be very sensitive to this density ratio. Since the pressure distribution and the drag coefficient depend on the location and configuration of this shock, it is believed that reliable extrapolation to flight conditions cannot be obtained without reasonable simulation of normal shock density ratio. Most facilities that use air or nitrogen as the test gas cannot provide the required simulation of normal shock density ratios.

## INTRODUCTION

Studies are currently being made of suitable entry configurations for an unmanned Mars mission. One of the purposes of this mission would be to land a scientific payload on the surface of Mars. Such an entry configuration must have low values for the ballistic coefficient in order to utilize atmospheric braking in the thin Martian atmosphere.

One class of shapes desirable from a structural standpoint (ref. 1) is a bell shape known as a tension shell. The structural advantages of this shape are discussed in reference 2. Previous aerodynamic studies (refs. 3 to 6) have shown that such shapes may have extensive regions of separated flow. The extent and stability of the separated flow are dependent on Reynolds number, wall-to-total-temperature ratio, and angle of attack. Shape parameters, such as bluntness ratio and fineness ratio, also affect the flow configuration.

The present investigation was undertaken to determine the effect of wall-to-total-temperature ratio, Reynolds number, and angle of attack on the formation and extent of boundary-layer separation and to study the resulting flow fields about certain of these shapes.<sup>1</sup> Schlieren data were obtained on four preliminary shapes for ranges of free-stream Reynolds numbers based on model base diameter from  $0.106 \times 10^6$  to  $1.36 \times 10^6$ , wall-to-total-temperature ratios from 0.2 to 0.9, and angles of attack from  $0^\circ$  to  $31^\circ$ . Based on the results for these preliminary configurations, a shape was selected that seemed to have steady flow and high drag for a wide range of conditions. Pressure and heat-transfer distributions were obtained for this "improved" shape at wall-to-total-temperature ratios of approximately 0.9 and 0.5, respectively, angle of attack from  $0^\circ$  to  $20^\circ$ , and free-stream Reynolds numbers based on base diameter of  $0.2 \times 10^6$  and  $0.5 \times 10^6$ . The effect of normal shock density ratio on the flow field was investigated briefly for this shape in a small hypersonic facility using  $\text{CF}_4$  (tetrafluoromethane) as the test gas.

## SYMBOLS

a,b,c,d	flow regions (see fig. 15)
D	base diameter
h	heat-transfer coefficient
$h_0$	reference heat-transfer coefficient taken to be the calculated value at the stagnation point of a sphere having same diameter as model base
$M_\infty$	nominal free-stream Mach number

---

<sup>1</sup>A preliminary summary of the work presented herein was included in the informal discussions attendant to the AIAA Entry Technology Conference, Williamsburg, Va., Oct. 12-14, 1964.



$p$	local static pressure
$p_t$	total pressure behind a normal shock
$r$	local body radius
$r_c$	corner radius at model base
$r_n$	nose radius
$R_{\infty,D}$	free-stream Reynolds number based on model base diameter
$T_w$	wall temperature
$T_t$	total temperature
$x$	distance along axis of symmetry of model (see fig. 1)
$\alpha$	angle of attack
$\Delta$	shock standoff distance (see fig. 19)
$\rho_s$	density behind normal shock
$\rho_{\infty}$	free-stream density
$\phi$	circumferential angle measured from windward ray of model

## APPARATUS

This investigation was conducted in the Langley Mach 8 variable-density tunnel. (See ref. 7 for detailed description.) This tunnel is of the blowdown type and has an axially symmetric nozzle with contoured walls. The average test section Mach number variation with stagnation pressure is given in reference 8 and varies from 7.6 to 7.96 for the conditions of the present tests. These conditions were stagnation pressure from 65 to 1015 psia (0.447 to 7.0 MN/m<sup>2</sup>) and stagnation temperature from 800° F to 1000° F (700° K to 812° K). The free-stream Reynolds number range of the present tests was from  $0.106 \times 10^6$  to  $1.5 \times 10^6$ , based on model base diameter.

The CF<sub>4</sub> (tetrafluoromethane) facility was a small blowdown wind tunnel having a conical nozzle with a 3-inch (7.63-cm) diameter test section. It operated over a range of stagnation pressures from 1000 to 2500 psia (6.89 to 17.2 MN/m<sup>2</sup>) at a stagnation temperature of approximately 350° F (450° K). The free-stream Mach number was approximately 8.

## MODELS AND INSTRUMENTATION

The external coordinates of the four preliminary configurations are shown in figure 1. Two sets of models were made: one set with  $D = 4$  inches (10.16 cm)

and one set with  $D = 2$  inches (5.08 cm). These models were machined from 347 stainless steel and had a sharp corner at the intersection of the flared base and the aft ring (fig. 1).

Shown in figure 2 are the coordinates for the final configurations tested in the present investigation, models 5 and 6. Pressure and heat-transfer models were constructed with both sharp and blunt noses, as shown in the figure. Beryllium copper was used for the pressure models, with 0.030-inch (0.076-cm) diameter orifices installed at the surface coordinates given in the figure. All orifices were located along one ray of the model. A copper-constantan thermocouple was installed in the position shown in figure 2 to indicate wall temperature. Heat-transfer models were cast from a high temperature plastic. The sharp nose of the heat-transfer model was made of steel (1/2 inch (1.27 cm) in length) to ensure a sharp tip during the tests.

The preliminary shapes with the 4-inch (10.15-cm) base diameter were tested with cooled-wall conditions. Liquid nitrogen was sprayed into an interior cavity by means of the nozzle shown in figure 3. During the cooling and testing periods the model was clamped onto the strut with the end of the nozzle inserted inside the cavity about 1/2 inch (1.27 cm) from the back surface of the model. The liquid nitrogen vaporized and passed into the wake of the model. Thermocouples were located on the back surface of the model to indicate wall temperature.

#### EQUIPMENT

Photographs of the flow fields of the preliminary configurations were obtained at zero angle of attack during tests with both cooled- and uncooled-wall conditions. A single pass schlieren system and a 16-mm motion-picture camera were used with a framing speed of 200 frames/sec and an exposure time of 2.2 milliseconds. A dc power supply was used for the light source. Schlieren photographs for angles of attack greater than zero were obtained by using an aerographic camera and a schlieren spark exposure time of 4 to 6 microseconds.

Motion pictures of the phase-change coating used in obtaining the heat-transfer data were taken with a 35-mm camera at a framing speed of 20 frames/sec and electronic strobe lights.

The pressure data were recorded photographically from mercury manometers.

#### TEST PROCEDURES AND DATA REDUCTION

All tests were conducted by injecting the model into the tunnel test section after the flow was established. The total time for injection was approximately 0.1 second.

## Schlieren Photographs

Preliminary configurations.- The 4-inch (10.15-cm) diameter models were tested at zero angle of attack with both the cooled- and uncooled-wall conditions which gave initial values of  $T_w/T_t$  of approximately 0.2 and 0.4, respectively. The motion-picture camera was started just before the models were injected into the stream to ensure that data were obtained with the wall temperature essentially at its initial value. For the uncooled-wall conditions, pictures were taken with an aerographic camera at angles of attack of  $0^\circ$ ,  $8^\circ$ ,  $15^\circ$ , and  $31^\circ$ . Because of a delay of approximately 5 seconds between successive photographs at a constant angle of attack the model wall was generally warmer than its initial value. Therefore  $T_w/T_t$  varied from about 0.4 to 0.9 for these photographs depending upon test time. The 2-inch (5.08-cm) diameter models were tested only at zero angle of attack with the uncooled-wall conditions. Motion pictures were taken of these tests. The Reynolds number range of these tests on the preliminary configurations was from  $0.106 \times 10^6$  to  $1.36 \times 10^6$ .

Final configurations.- Schlieren data for the final configurations were obtained at Reynolds numbers of  $0.2 \times 10^6$ ,  $0.5 \times 10^6$ , and  $1.5 \times 10^6$  for a wall temperature near room temperature ( $T_w/T_t \approx 0.4$ ). The wall temperature measured at the thermocouple location shown in figure 2 was used to obtain the ratio  $T_w/T_t$  for these tests.

## Pressure Distributions

Pressures on the final configuration beryllium copper models were obtained at Reynolds numbers of  $0.5 \times 10^6$  and  $1.4 \times 10^6$  for the uncooled-wall conditions. The ratio  $T_w/T_t$  was approximately 0.9 because of the time required for the settling of the mercury manometers.

## Heat-Transfer Distributions

The heat-transfer tests were made only for the final configurations (models 5 and 6) at  $R_{\infty,D} = 0.2 \times 10^6$  with an uncooled wall ( $T_w/T_t \approx 0.5$ ). Heat-transfer data were obtained by a phase-change coating technique described in references 9 and 10. The coatings used had phase-change temperatures of  $125^\circ\text{F}$  and  $250^\circ\text{F}$  ( $325^\circ\text{K}$  and  $395^\circ\text{K}$ ). In this technique the heat-transfer coefficients are determined by measuring the time required for a point on the surface of the model to reach the phase-change temperature, as indicated by the visible phase change of a thin surface coating. These values of time and temperature are then used in the solution to the heat conduction equation for a semi-infinite slab with a step input in  $h$  to ascertain the heat-transfer coefficient.

## ACCURACY

The accuracy of the phase-change coating technique is discussed in detail in reference 10. For the present tests the final heat-transfer coefficient data are probably accurate to within 15 percent.

The accuracy of the pressure data is determined primarily by the accuracy to which the manometer data can be read from the film. For the present tests the maximum error is about  $\pm 5$  percent.

The wall temperature was taken to be that indicated on the back surface of the model at the thermocouple location shown in figures 2 and 3. Even though the model material was a good thermal conductor there was a temperature distribution along the surface as well as some difference between the front and back surface temperatures. Therefore, the wall temperatures given for the schlieren and pressure studies are only approximate. The estimated accuracy of the ratio  $T_w/T_t$  is  $\pm 0.05$ .

## RESULTS AND DISCUSSION

### Preliminary Configurations

Uncooled-wall conditions.- Shown in figures 4 to 7 are schlieren photographs of the four preliminary models for the uncooled-wall condition ( $T_w/T_t \approx 0.5$ ). Photographs are shown at various values of  $R_{\infty,D}$  and for  $\alpha = 0^\circ, 8^\circ, 15^\circ$ , and  $31^\circ$  and illustrate the effect of  $R_{\infty,D}$  and  $\alpha$  upon shock shape and flow-field stability. To illustrate unsteady flow fields, two schlieren pictures at the same Reynolds number are sometimes shown. When the flow field is similar to that of another Reynolds number and both appear steady, only one photograph is shown. Examination of successive photographs taken for fixed stream conditions aided in the determination of whether the flow was steady or unsteady. Both the motion-picture films and the spark photographs seemed to give similar results, even though the wall temperature for the latter was greater than the initial value. These remarks, therefore, are valid for  $T_w/T_t \approx 0.5$ .

The results for preliminary model number 1 are shown in figure 4. At zero angle of attack and low Reynolds number the flow around the model is unsteady with extensive regions of separated flow. Increasing the Reynolds number reduces the extent of separation, stabilizes the flow, and results in a higher drag flow pattern (refs. 6 and 11). The same general trend occurs at angle of attack.

Results for model 2 are shown in figure 5. For this model, at zero angle of attack, increasing the Reynolds number stabilized the flow, but did not appreciably affect the extent of flow separation.

Figures 6 and 7 are the results for models 3 and 4, respectively, and show the opposite trend, in respect to the effect of Reynolds number on relative

stability, from models 1 and 2. As Reynolds number is increased the flow seems to become more unsteady. However, the flow-field fluctuations are of smaller amplitude than those which occur for models 1 and 2. The extent of separated flow over these configurations does not seem to change appreciably with Reynolds number. These remarks apply also for the models at angle of attack.

The previous discussion indicates that for the uncooled wall there are two different types of flow about these shapes. The separated flow field for a shape having a small ratio of  $r_n/D$  (models 1 and 2) seems to become stable at higher Reynolds numbers. Shapes having a larger value for  $r_n/D$  (models 3 and 4) seem to have unstable flow fields at higher Reynolds numbers.

To ensure that the instabilities noted at low Reynolds numbers on models 1 and 2 were not due to tunnel blockage effects, models of 2-inch (5.08-cm) base diameter were tested. For similar values of  $R_{\infty,D}$ , the same degree of fluctuation was noted in the shock shape; therefore, it is concluded that the observed flow-field fluctuations were not due to tunnel effects.

Cooled-wall conditions.- Shown in figure 8 are typical schlieren photographs taken with the motion-picture camera for  $\alpha = 0^\circ$  and  $T_w/T_t = 0.2$  for models 1 to 4. Similar trends with Reynolds number were apparent, as with the uncooled wall, for models 3 and 4, and there seemed to be little effect of cooling the wall. For models 1 and 2, however, cooling the wall seemed to stabilize the flow field at a lower Reynolds number. An entirely different (high-drag) flow pattern was observed for model 2 at  $R_{\infty,D} = 1.36 \times 10^6$ , whereas for the uncooled wall tests it was not observed (see fig. 5(a)); a similar effect of wall temperature upon extent of separated flow was observed on similar configurations in reference 5. As some degree of nose blunting will probably occur during Martian entry, it is advantageous that this high-drag shock shape occur for model 2 as well as for model 1. The value of  $T_w/T_t$  for these tests was 0.2 and is thought to be a conservative estimate for an actual entry. However, the high-drag shock shape only occurs for the high Reynolds number test.

Corner radius effect.- To ascertain if changing the shape of the rear corner would promote the formation of the high-drag flow field at lower Reynolds numbers, a 0.12-inch (0.305-cm) radius ( $r_c/D = 0.03$ ) was machined on the rear corner of model 2. This model was then tested with both a cooled and uncooled wall and over the same Reynolds number range as before. The results of these and the previous tests are summarized in figure 9. This figure shows the effect of  $T_w/T_t$  and  $R_{\infty,D}$  on shock shape for both the sharp and round corner models. These data were obtained by suddenly exposing a cold model to the airstream and observing the flow field as the model was heated during the run. The model temperature at which a change in flow field occurred was recorded. The approximate region where the flow field changed is shown as a band because of the limited number of tests conducted and the uncertainty in the value of  $T_w/T_t$ . The flow field to the upper left of a band is characterized by extensive boundary-layer separation, which streamlines the flow and results in a shock wave similar to that about a blunted cone, and is, consequently, a lower drag flow pattern. The flow field to the lower right of a band is characterized by attached boundary-layer flow with a nearly isentropic compression downstream of

the nose, a large nearly normal shock, very high pressures over the large area of the flare, and consequently high drag. It can be seen from this figure that rounding the back corner caused the high-drag shock shape to be maintained at lower values of Reynolds number even for relatively hot walls. Rounding the corner also affected the stability of the flow field for model 2. This effect can be seen by comparing figures 9 and 10. For the sharp corner tests (fig. 10) a region of unsteady flow was observed for the low-drag shock shape, whereas for the round corner (fig. 9) unsteady flow was never observed for the conditions of the present tests. Therefore, a rounded corner design makes it possible to obtain the high-drag steady flow field around a blunt-nose body even for the low initial Reynolds number at the low values of  $T_w/T_t$  that would occur during Martian entry.

### Final Configuration

On the basis of the aforementioned results a shape was chosen that would give the desired high-drag flow field for a wide range of Reynolds numbers and  $T_w/T_t$ . This shape (see fig. 2) was slightly longer than model 2 and had the same corner radius at the flare as model 2 with a rounded corner.

Schlieren study.- Presented in figures 11 and 12 are schlieren photographs of models 5 and 6 for uncooled-wall conditions ( $T_w/T_t \approx 0.5$  to  $0.8$ ), Reynolds numbers of  $0.2$ ,  $0.5$ , and  $1.5 \times 10^6$ , and angles of attack of  $0^\circ$ ,  $5^\circ$ ,  $12^\circ$ , and  $20^\circ$ . Data for both a sharp and blunt configuration are presented. The photographs were taken at the beginning of the test and since the model material (beryllium copper) is a good thermal conductor the model was essentially isothermal.

Shown in figure 11 are schlieren photographs of the sharp-nose model at  $\alpha = 0^\circ$ ,  $5^\circ$ ,  $12^\circ$ , and  $20^\circ$ . Only one picture was taken during a given test and therefore nothing can be said as to relative stability of the flow field about this configuration except that in visual observation it appeared to be steady. At zero angle of attack the flow field is the high-drag type with a relatively small separated flow region where the nearly normal flare shock originates near the body. The extent of this separation decreases with increasing Reynolds number for all values of  $\alpha$ .

Shown in figure 12 are schlieren photographs for the blunt-nose configuration. The flow-field results for the final configuration are in agreement with the flow-field map for model 2 with the rounded corner (see fig. 9) in that for a  $T_w/T_t$  of approximately  $0.5$  to  $0.6$  the flow was attached (high drag) for  $R_{\infty,D} > 0.4 \times 10^6$  and becomes separated (low drag) for  $R_{\infty,D} < 0.3 \times 10^6$ . However, the flow does not become attached on the lee side of the blunt model with increasing  $R_{\infty,D}$  at angle of attack as it did for the sharp-nose final configuration at small angles of attack.

Pressure distributions.- Shown in figure 13 are the measured pressure distributions for the sharp-nose final configuration for angles of attack of  $0^\circ$ ,  $5^\circ$ ,  $12^\circ$ , and  $20^\circ$ . Pressure distributions for the blunt-nose final configuration are presented in figure 14. For both sets of data the measured local surface pressure has been nondimensionalized by dividing by the calculated

stagnation pressure behind a normal shock at the nominal free-stream Mach number (that is, free-stream pitot pressure). All the data in these two figures were taken at nearly adiabatic wall temperature since long testing times were required to settle out the manometers.

The zero angle-of-attack pressure distribution of the sharp-nose configuration is shown in figure 13(a). The model is conical in the vicinity of the nose ( $r/D < 0.12$ ) with a half angle of  $28^\circ$ , and the pressures in this region are in agreement with cone theory (ref. 12). Downstream of this region the pressure increases in a uniform manner up to the vicinity of the flare-shock skirt-shock juncture ( $r/D \approx 0.23$ ). Downstream of this intersection there is a sudden large increase in pressure with a peak more than twice the free-stream pitot pressure. The data for locations downstream of  $r/D = 0.27$  show a series of alternating high and low pressures with the general pressure level in excess of the pitot pressure.

Some of the same trends were found at angle of attack, for example, the alternating high and low pressures on the flare. However, the peak pressure was not always on the windward ray. At  $\alpha = 12^\circ$  (fig. 13(d)) the peak pressure occurred at  $\phi = 120^\circ$ . For angles of attack of  $12^\circ$  and  $20^\circ$  the leeward ray ( $\phi = 180^\circ$ ) had a much lower pressure level than the other rays. This lower pressure is probably due to extensive boundary-layer separation on the lee side. In general, the blunt configuration (fig. 14) showed the same trends as the sharp configuration.

The effect of Reynolds number on pressure distribution can be seen by comparing figures 13(a) and 13(b) or figures 14(a) and 14(b). As is indicated in these figures there is no effect of Reynolds number on the cone-shock skirt-shock intersection; however, at the higher Reynolds numbers the point of reflection of the first imbedded shock moves forward slightly. This shift is probably due to boundary-layer displacement effects.

When comparing pressure distributions for the sharp and blunt configurations it should be noted that the pressure orifices are in fixed locations. In other words, for distributions with sharp peaks, only a small shift of the point of shock impingement on the body is required to miss a value at the peak pressure. Therefore, no great significance can be placed on the differences in magnitude of the peak-measured pressures in figures 13 and 14, but in general the peak-measured pressures are a maximum for the sharp configuration.

The data for various angles of attack are shown in figures 13(c), 13(d), 13(e), 14(c), 14(d), and 14(e) at roll angles from  $0^\circ$  to  $180^\circ$ . As expected from the schlieren photographs of figure 11, the windward ray has a distribution which exhibits the same characteristics as those for zero angle of attack; whereas on the lee side there is more separation, particularly at higher angles of attack, and consequently a smoother distribution.

Flow field.— It is of interest to determine if details of the flow field for the sharp configuration at zero angle of attack as seen in the schlieren photograph of figure 11(a) correlate with the pressure distribution of figure 13(a). At these conditions the extent of separated flow is very small and

the surface pressure distribution depends mainly on the inviscid flow properties. A sketch of the schlieren photograph of figure 11 ( $R_{\infty,D} = 0.5 \times 10^6$ ) is given in figure 15 to clarify the nature of the flow field. Downstream of the conical portion ( $0.12 < r/D < 0.23$ ) the pressure rises gradually as the flow is being turned in what is essentially an isentropic process.

Farther downstream a large nearly normal shock intersects the nearly conical shock from the forward portion of the model. This shock is labeled the skirt shock in figure 15 and the intersection of the forebody shock and the skirt shock occurs at an  $x/D$  of about 0.2 which corresponds to a surface location of  $r/D = 0.23$  in figure 13(a) (taken as surface location beneath the shock intersection along a line normal to the axis). From this point rearward the flow field is considerably more complicated. Immediately behind the skirt shock, region c, is a subsonic constant pressure region with a static pressure close to normal shock recovery pressure. This phenomenon imposes a constant pressure boundary on the lower entropy flow along the model surface, regions a, b, and d, which remains supersonic as far downstream as  $r/D = 0.40$ . The constant pressure boundary is a slip flow line or vortex sheet separating regions c and b. As the lower entropy flow in region a moves downstream it must turn so as to produce an increase in static pressure to the level prevailing in region c. Consequently, an oblique shock is formed between regions a and b. This shock is reflected from the surface at  $r/D = 0.27$ . Behind the reflected shock (region d) the flow is still supersonic but at a very high static pressure. From figure 13(a) the pressure in region d was found to be as high as 2.2 times the free-stream pitot pressure. When the reflected shock reaches the constant pressure boundary or slip flow line the flow must expand so as to reach a static pressure again equal to that in region c. The expansion fan intersects the model surface near  $r/D = 0.325$  and reduces surface pressures very sharply. Therefore the flow between the vortex sheet and the body surface is characterized by an alternating series of reflected shocks and expansions until finally, somewhere downstream of  $r/D = 0.40$ , the vortex sheet is dissipated and pressures are equalized with uniform subsonic flow occurring along the surface. This alternating series of reflected shocks and expansions results in widely varying surface pressures over the rear of the model with regions where the static pressure is far in excess of the free-stream pitot pressure and regions where pressure is below the free-stream pitot pressure.

On the basis of the flow mechanisms just described, an approximate calculation for the surface pressure distribution can be carried out as follows: First, neglecting boundary-layer separation, assume that the flow initially passes through a conical shock with a flow deflection equal to the initial cone angle of the model. Then assume that the flow is compressed isentropically and use the method of characteristics in this isentropic compression region. Finding the intersection of the strong nearly normal skirt shock and the forebody shock requires a double iteration. Arbitrarily assume a point of intersection. The fact that the pressures and flow angles behind the intersection must be equal requires a slip discontinuity because of the different velocities and entropies. The strong skirt shock requires subsonic flow behind it with one of three possible flow patterns between the slip line and the surface: (1) an oblique compression shock which is reflected from the surface and followed by an expansion; (2) a normal compression shock followed by subsonic flow; or (3) a simple



expansion fan followed by an oblique shock. The particular pattern which satisfies the equal pressure requirement between regions b and c depends on the free-stream conditions and the assumed location of the intersection point. When the required equality of flow angle and pressure between regions b and c are satisfied, the inclination of the skirt shock is uniquely specified. Determine the shape of the rest of the skirt shock from an empirical correlation of measured shock shape. Then verify the intersection point by a trial-and-error procedure in which the mass flow passing in through the skirt shock is in balance with that passing outward between the slip flow line and the skirt shock at the rear of the body. For this mass balance, constant pressure is assumed between the skirt shock and slipline.

The preceding is a description of the basic elements of a flow-field analysis which was presented in reference 13 in which a surface pressure distribution was calculated for the same shape and free-stream conditions as that of figure 13(a). The results of this calculation are presented in figure 16 and compared with the measured pressure distribution of figure 13(a). This approximate theory predicts accurately the location of the first large pressure rise as well as its magnitude and the distribution in the isentropic compression region.

Effect of normal shock density ratio.- A flow-field calculation was made in reference 13 for equilibrium flow in a postulated Mars atmospheric composition at high velocities. The assumed free-stream conditions resulted in a density ratio across a normal shock of  $\rho_s/\rho_\infty = 16.7$  as compared with  $\rho_s/\rho_\infty = 5.57$  for the ideal gas calculation in air at Mach 8 which is shown in figure 16. These results are reproduced in figures 17 and 18 in order to illustrate the sensitiveness of the flow field over the sharp-nose model to real gas effects, primarily the density ratio. As shown by comparing figures 15 and 17, the large skirt shock moves rearward by a considerable amount because of the increase in  $\rho_s/\rho_\infty$  and consequently the large peak in surface pressure moves rearward also (fig. 18). Under these particular real gas conditions an expansion fan is required in order to meet the equal pressure condition across the slip boundary generated at the intersection of the forebody shock and the skirt shock (pattern (3) discussed earlier).

These results indicate that the flow field, pressure distribution, and, therefore, the center of pressure and force and moment coefficients or stability coefficients for this configuration are highly sensitive to real gas effects, primarily the shock density ratio. Since the flow field is also very sensitive to boundary-layer separation and therefore sensitive to Reynolds number and wall cooling effects, it is very difficult to extrapolate ground test results to flight conditions. Any possible structural weight advantages of these tension shell shapes will be largely offset by these unpredictable and generally poor aerodynamic characteristics.

In order to verify experimentally the dependence of the skirt-shock location on density ratio  $\rho_s/\rho_\infty$ , a few tests were made in a small hypersonic facility with  $\text{CF}_4$  as the test gas. The free-stream Mach number was approximately 8. Because of the low specific heat ratio of  $\text{CF}_4$  a much larger density ratio occurs across a normal shock than for the Mach 8 air tests. This density

ratio was determined to be about 10 by measuring the shock standoff distance at the stagnation point of a sphere and by using the relation

$$\frac{\Delta}{D} = 0.4 \frac{\rho_{\infty}}{\rho_s}$$

which is a fit to the theoretical and experimental data of references 14 and 15. A spark shadowgraph of the flow about the final configuration in this CF<sub>4</sub> facility is shown in figure 19 along with a sketch defining  $\Delta$  and  $D$ . For the air tests where the density ratio was 5.6 the shock standoff distance is much larger ( $\Delta/D = 0.21$ ) than that for the CF<sub>4</sub> tests where the density ratio was 10 ( $\Delta/D = 0.14$ ). These results indicate that the use of CF<sub>4</sub> as a test gas in a hypersonic facility may be desirable as a way of simulating the normal shock density ratios and resulting shock shapes that occur during high-speed flight where real gas effects give very different density ratios than those of ideal gas facilities using air.

Heat-transfer distributions.— Heat-transfer distributions were measured by using the technique described in references 9 and 10. All heat-transfer data were obtained at Reynolds numbers based on free-stream conditions and base diameter of approximately  $0.2 \times 10^6$ . Coatings having phase-change temperatures of 125° F and 250° F (325° K and 394° K) were used and, since the initial temperature of the model was always near room temperature, the temperature change of the model surface was relatively small during testing. The total temperature was approximately 900° F (756° K) so that the ratio  $\Delta T_w/T_t$  ( $\Delta T_w = T_{w, \text{initial}} - T_{w, \text{phase change}}$ ) varied from 0.033 to 0.13 for these tests whereas  $T_w/T_t$  was approximately 0.4 to 0.5.

Representative photographs showing phase-change patterns of the sharp model made from films taken during these tests are shown in figures 20 to 22. These photographs are numbered to show the time sequence in which they were taken. Phase-change patterns for the sharp model at zero angle of attack are shown in figure 20. The coated model before any phase change has occurred appears white. After a phase change the coating is transparent and the dark surface of the model is visible. The lines separating the light and dark areas are locations at which a phase change was occurring and are therefore at a known temperature. Since the sharp nose was made of steel it had a much greater heat capacity and conductivity than the plastic and no useful data could be obtained in this region. Also, for an equal heat-transfer coefficient, it took much longer for a phase change to occur on the steel surface than on the plastic. As a result, even though the heating rates near the sharp tip are high compared with those in the other areas, no phase change has taken place at this point until a much later time. The patterns shown in figure 20 indicate a small band of very high heating at the approximate location of the peak pressure. These patterns also show that the heat-transfer coefficient on the entire flare is much larger than that on the forward portion.

The phase-change patterns for the windward side at  $\alpha = 12^\circ$  are shown in figure 22. At this test condition the phase-change patterns indicate two narrow bands close together with higher heating rates than those in the surrounding area.

Heat-transfer coefficient distributions are presented in figures 23 to 26. The lines in figures 23 to 26 represent faired curves of the data. For the blunt configuration the data are faired into the calculated values for the spherical stagnation region; these calculated values are shown as a dashed line. The local measured heat-transfer coefficient  $h$  has been nondimensionalized by dividing by the calculated heat-transfer coefficient at the stagnation point of a reference sphere, which has a radius equal to the model base radius. This reference heat-transfer coefficient  $h_0$  was calculated by the method of reference 16 using a Newtonian velocity gradient. The distribution for the sharp model at zero angle of attack is shown in figure 23. A maximum heat-transfer ratio of 3.4 was reached at a location of  $r/D \approx 0.34$  which is somewhat downstream of the peak pressure location of figure 13(a). However, the pressure data were taken at a higher Reynolds number than that for the heat-transfer data. The wall-to-total-temperature ratios were different and, because of the discrete spacing of the pressure orifices, the peak pressure may have been at a slightly different location than that at which the data of figure 13(a) were taken. Therefore, only a general comparison between the pressure and heat-transfer distribution is possible. Such a general comparison indicates that the pressure and heat-transfer distributions are somewhat similar in that both have wide variations in the value with surface distance and that the peak pressures are in the same approximate location as the high heat-transfer rates. For the blunt model at zero angle of attack the boundary layer is separated from a region just downstream of the nose to the base, and the heat-transfer distribution (fig. 24) is smoother with the maximum measured values near the base at  $r/D \approx 0.47$ .

Figures 25 and 26 present measured heat-transfer distributions for the sharp model at angles of attack of  $5^\circ$  and  $12^\circ$ , respectively. No data are presented for the blunt model at angle of attack since the flow field changed with the wall-to-total-temperature ratio for wall temperatures between room temperature and the phase-change temperature of the coating. This sensitiveness to wall-to-total-temperature ratio in the temperature range of these tests resulted in a variation of heat-transfer coefficient with time and, consequently, the phase-change method, which assumes an invariant heat-transfer coefficient, is invalid. In general, the heat-transfer distributions at angle of attack are irregular on the windward side with sharp peaks in locations downstream of the cone-shock skirt-shock intersection whereas the leeward side has a more gradual variation.

#### CONCLUDING REMARKS

An experimental investigation of the flow field, pressure distributions, and heat-transfer distribution for several tension shell configurations at a Mach number of 8 has been made and is summarized in the following paragraphs:

For these configurations boundary-layer separation plays an important role in the observed flow-field phenomena. In general, two different flow-field configurations were observed. For one flow configuration the boundary layer remained attached for some distance downstream of the nose, and farther downstream the flow passed through a large nearly normal shock. For the other type

of flow configuration the boundary layer separated just downstream of the nose and reattached on the edge of the flare.

The extent of separation and type of flow field were found to be functions of wall-to-total-temperature ratio, Reynolds number, and minor changes in body shape. A shape which appeared to have a steady attached boundary layer with a nearly normal flare shock (high drag) over a wide range of test conditions was studied more extensively. A criterion for distinguishing between the attached high-drag and separated low-drag flow fields was found for this shape.

The high-drag flow field produced a wide range of surface pressures with surface distance over the flare with peaks as high as 2.2 times the free-stream normal shock total pressure whereas minimum values were of the same order as this pressure.

A comparison of shock patterns for the high-drag configuration taken in air at Mach 8, where the normal shock density ratio was 5.6, with shock patterns obtained in  $\text{CF}_4$  (tetrafluoromethane) at a Mach number of about 8, where the normal shock density ratio was approximately 10, indicated that the location of the nearly normal flare shock is strongly dependent on the value of this density ratio.

These results show that the flow field and therefore the pressure and heating distribution, total drag, and stability coefficients for these shapes are very sensitive to Reynolds number, wall cooling effects, minor changes in body shape, and normal shock density ratio. The results also indicate that it will be extremely difficult to extrapolate ground test results obtained in air to flight conditions and that the structural weight advantages of these shapes will be largely offset by their unpredictable and generally poor aerodynamic characteristics.

Langley Research Center,  
National Aeronautics and Space Administration,  
Langley Station, Hampton, Va., September 28, 1966,  
124-07-02-60-23.

## REFERENCES

1. Roberts, Leonard: Entry Into Planetary Atmospheres. Astronaut. Aeron., vol. 2, no. 10, Oct. 1964, pp. 22-29.
2. Anderson, Melvin S.; Robinson, James C.; Bush, Harold G.; and Fralich, Robert W.: A Tension Shell Structure for Application to Entry Vehicles. NASA TN D-2675, 1965.
3. Bernot, Peter T.: Longitudinal Stability Characteristics of Several Proposed Planetary Entry Vehicles at Mach 6.73. NASA TN D-2785, 1965.
4. Centolanzi, Frank J.: Heat Transfer to Blunt Conical Bodies Having Cavities to Promote Separation. NASA TN D-1975, 1963.
5. Lankford, J. L.: The Effect of Heat Transfer on the Separation of Laminar Flow Over Axisymmetric Compression Surfaces - Preliminary Results at Mach Number 6.78. NAVWEPS Rept. 7402, U.S. Naval Ord. Lab., Mar. 17, 1961.
6. Robinson, James C.; and Jordan, Alfred W.: Exploratory Experimental Aerodynamic Investigation of Tension Shell Shapes at Mach 7. NASA TN D-2994, 1965.
7. Schaefer, William T., Jr.: Characteristics of Major Active Wind Tunnels at the Langley Research Center. NASA TM X-1130, 1965.
8. Stainback, P. Calvin: Heat-Transfer Measurements at a Mach Number of 8 in the Vicinity of a  $90^\circ$  Interior Corner Alined With the Free-Stream Velocity. NASA TN D-2417, 1964.
9. Jones, Robert A.; and Hunt, James L.: Use of Temperature-Sensitive Coatings for Obtaining Quantitative Aerodynamic Heat-Transfer Data. AIAA J., vol. 2, no. 7, July 1964, pp. 1354-1356.
10. Jones, Robert A.; and Hunt, James L.: Use of Fusible Temperature Indicators for Obtaining Quantitative Aerodynamic Heat-Transfer Data. NASA TR R-230, 1966.
11. Creel, Theodore R., Jr.: Longitudinal Aerodynamic Characteristics of a Tension Shell Entry Configuration at Mach 20. NASA TN D-3541, 1966.
12. Sims, Joseph L.: Tables for Supersonic Flow Around Right Circular Cones at Zero Angle of Attack. NASA SP-3004, 1964.
13. Anon.: Aeromechanics and Thermal Control. Vol. V, Book 2 of Comparative Studies of Conceptual Design and Qualification Procedures for a Mars Probe/Lander. AVSSD-0006-66-RR (Contract NAS 1-5224), AVCO Corp., May 11, 1966.

14. Van Dyke, Milton D.; and Gordon, Helen D.: Supersonic Flow Past a Family of Blunt Axisymmetric Bodies. NASA TR R-1, 1959.
15. Ridyard, Herbert W.; and Storer, Elsie M.: Stagnation-Point Shock Detachment of Blunt Bodies in Supersonic Flow. J. Aerospace Sci. (Readers' Forum), vol. 29, no. 6, June 1962, pp. 751-752.
16. Reshotko, Eli; and Cohen, Clarence B.: Heat Transfer at the Forward Stagnation Point of Blunt Bodies. NACA TN 3513, 1955.

Sharp corner

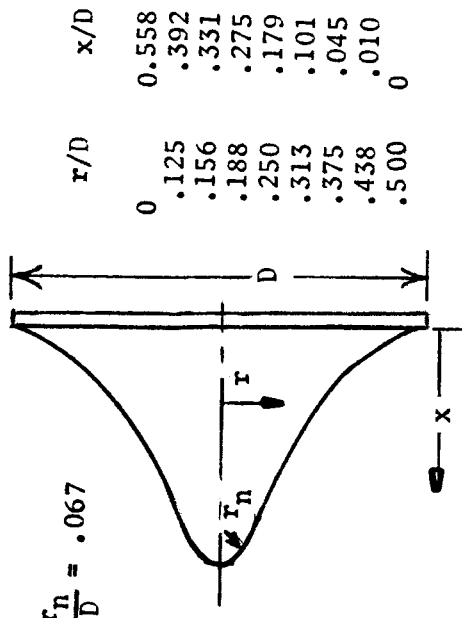
$r/D$	$x/D$
0	0.710
.05	.575
.10	.454
.15	.348
.20	.256
.25	.177
.30	.114
.35	.064
.40	.028
.45	.007
.50	0

Model 1

$r/D$	$x/D$
0	0.47
.125	.392
.156	.331
.188	.275
.250	.179
.313	.101
.375	.045
.438	.010
.500	0

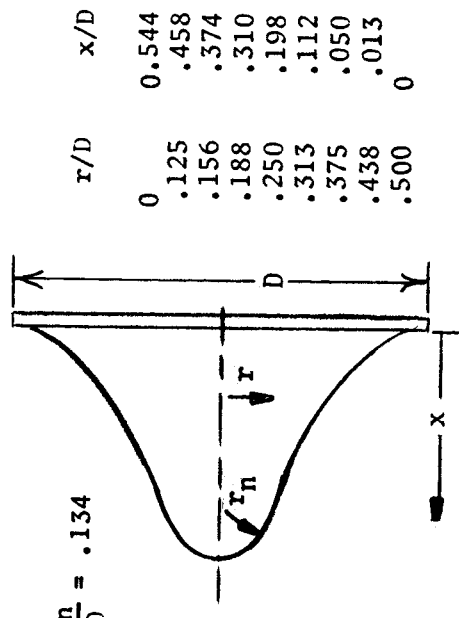
Model 3

$$\frac{r_n}{D} = .067$$



Model 2

$$\frac{r_n}{D} = .134$$



Model 4

Figure 1.- Sketch of preliminary configurations showing surface coordinates.  $D = 4$  in. (10.16 cm).

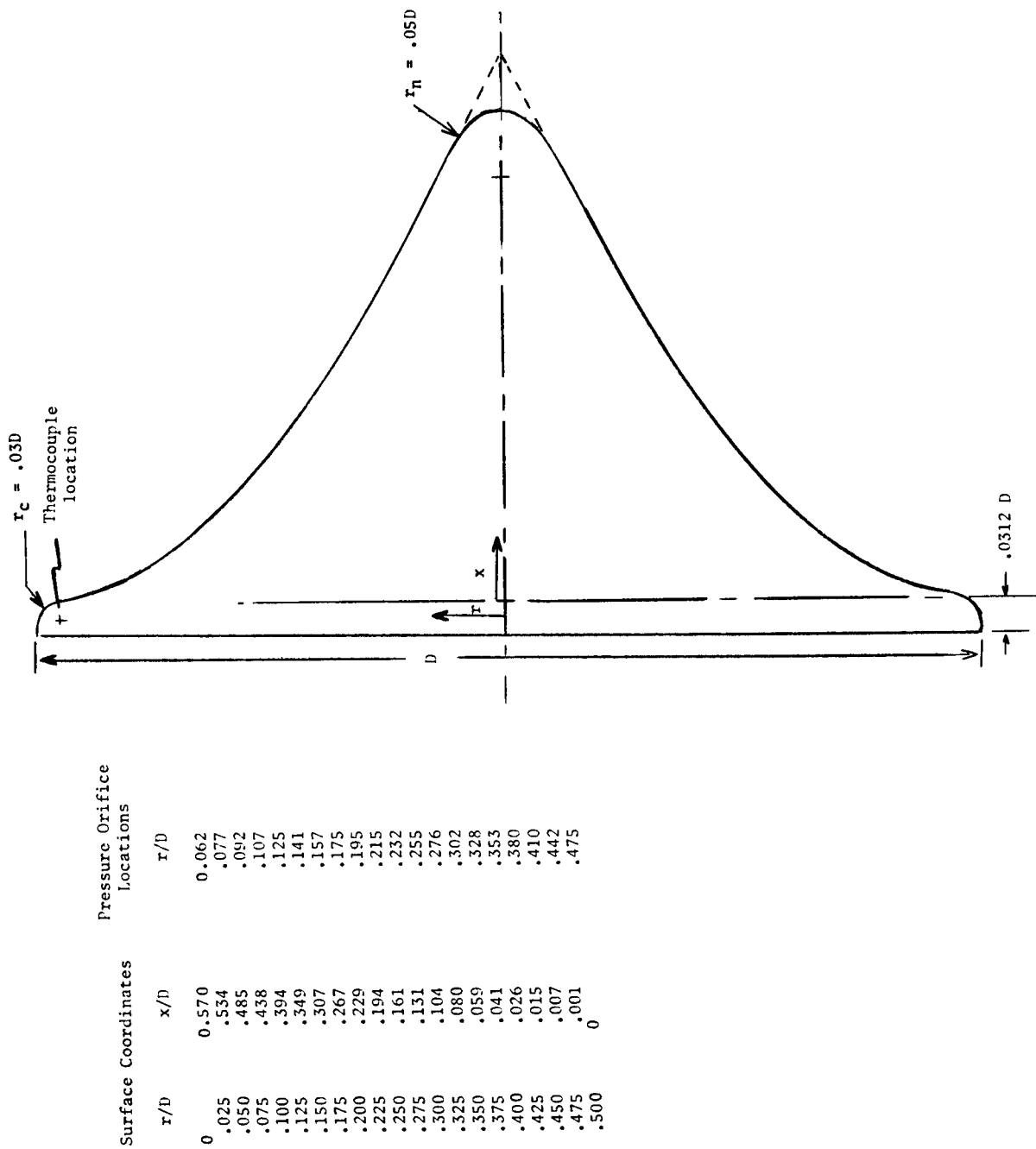


Figure 2.- Sketch of models 5 and 6 showing surface coordinates and pressure orifice locations.  $D = 4$  in. (10.16 cm).



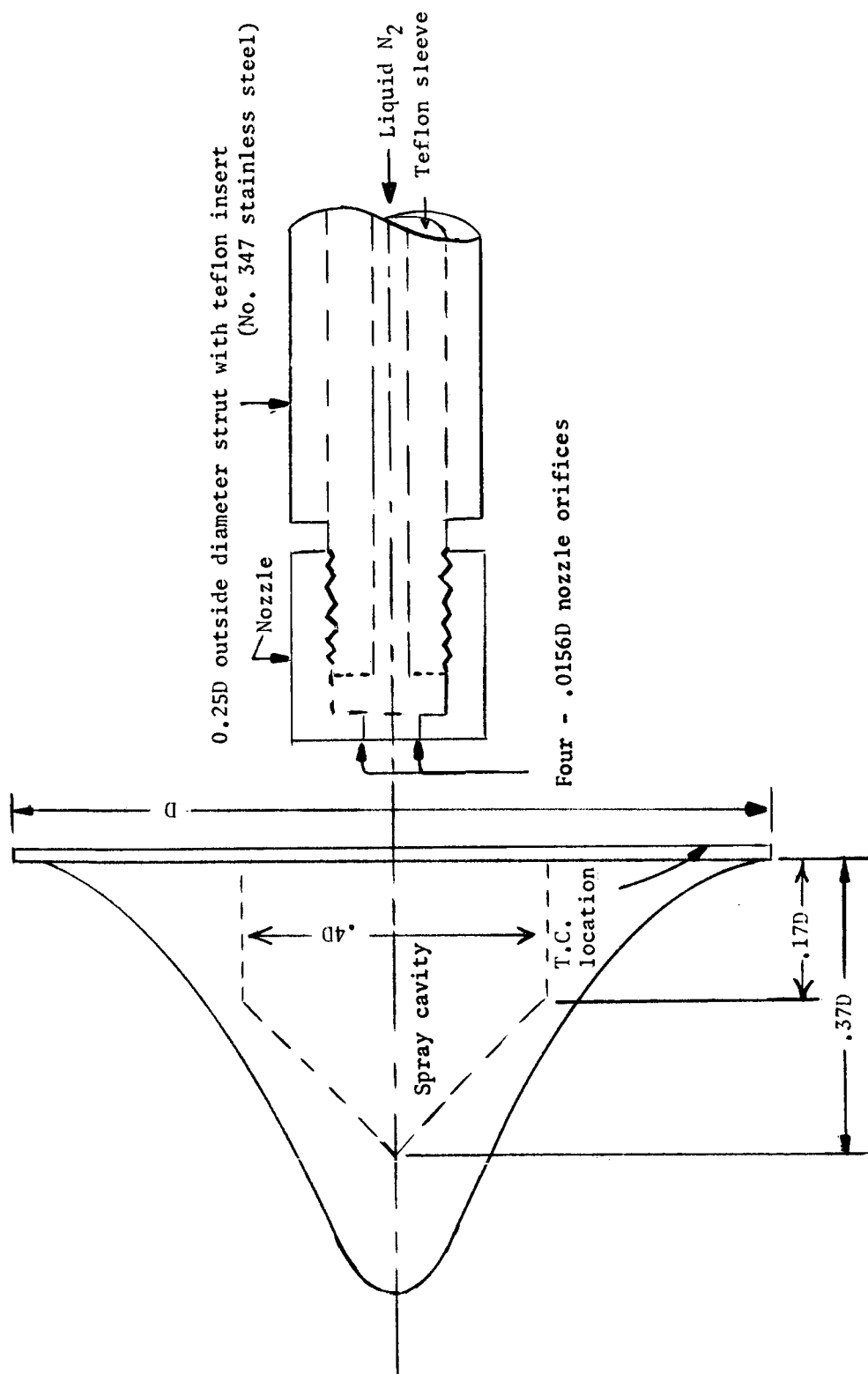
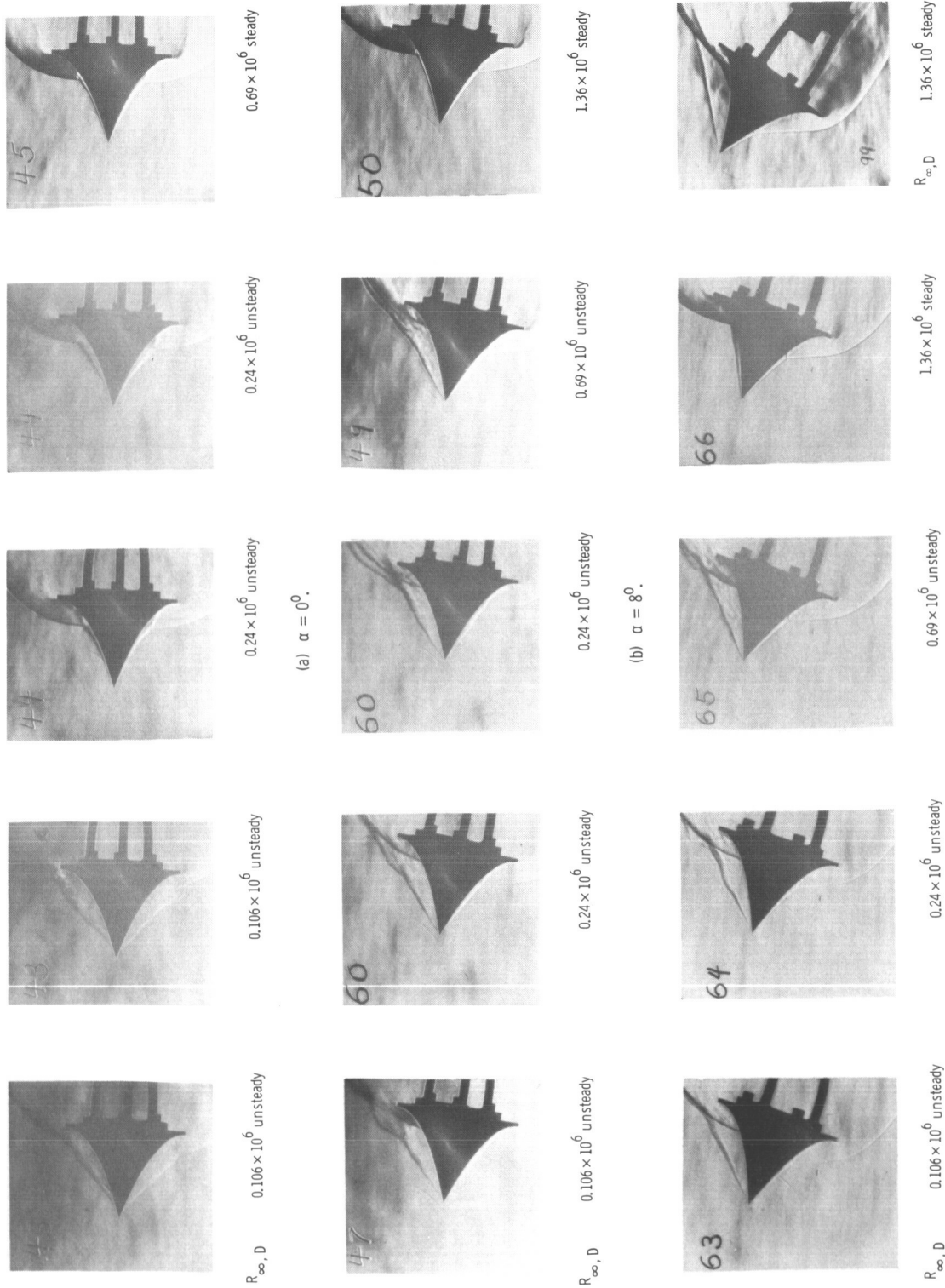


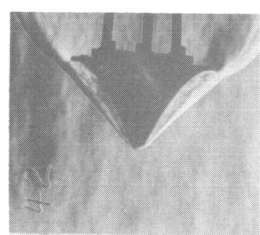
Figure 3.- Sketch of cooling system used with preliminary configurations.



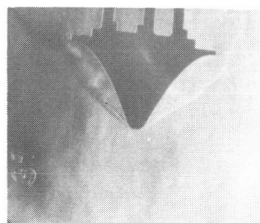
(c)  $\alpha = 15^\circ$ .

(d)  $\alpha = 31^\circ$ .

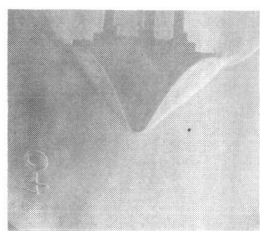
Figure 4.- Schlieren photographs of model 1 for the uncooled wall showing effect of Reynolds number and angle of attack upon flow field.  $T_w/T_t \approx 0.5$ ;  $M_\infty = 8$ ;  $r/D = 0$ . L-66-7612



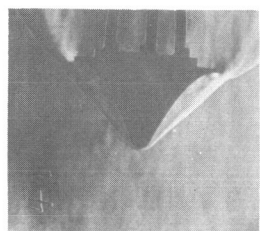
$R_{\infty, D}$        $0.106 \times 10^6$  unsteady



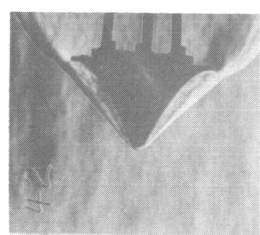
$0.106 \times 10^6$  unsteady



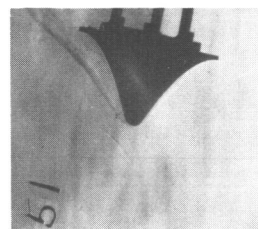
$0.24 \times 10^6$  unsteady



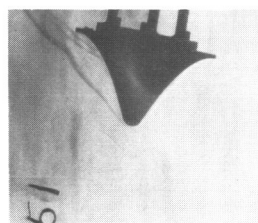
$0.69 \times 10^6$  unsteady



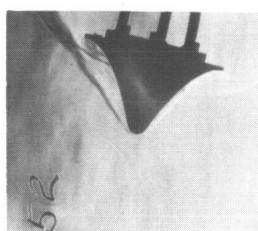
$1.36 \times 10^6$  steady



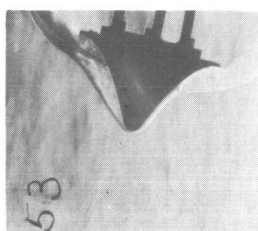
$R_{\infty, D}$        $0.106 \times 10^6$  unsteady



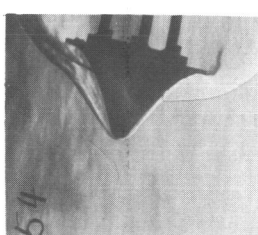
$0.106 \times 10^6$  unsteady



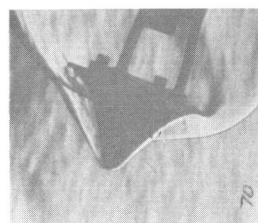
$0.24 \times 10^6$  unsteady



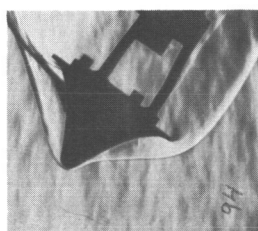
$0.69 \times 10^6$  steady



$1.36 \times 10^6$  steady



$R_{\infty, D}$        $1.36 \times 10^6$  steady



$R_{\infty, D}$        $1.36 \times 10^6$  steady

(c)  $\alpha = 15^\circ$

(d)  $\alpha = 31^\circ$

Figure 5.- Schlieren photographs of model 2 for the uncooled wall showing effect of Reynolds number and angle of attack upon flow field.  $T_w/T_t \approx 0.5$ ;  $M_\infty = 8$ ;  $r_\eta/D = 0.067$ .

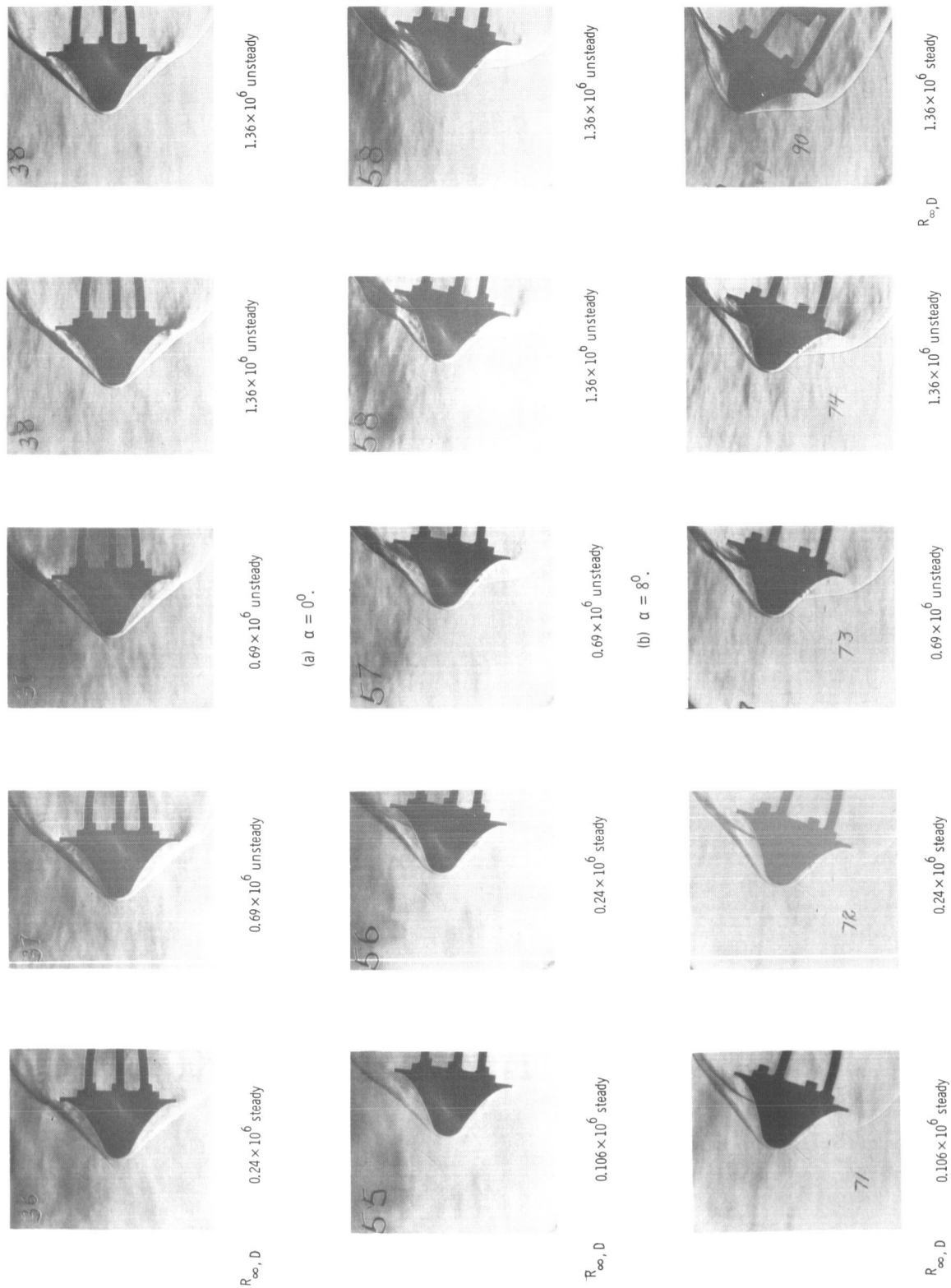
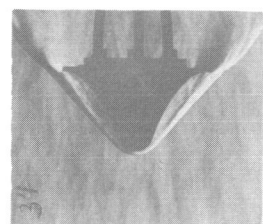
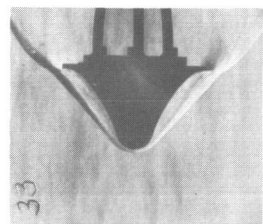


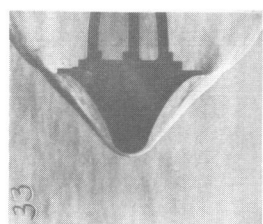
Figure 6.- Schlieren photographs of model 3 for the uncooled wall showing effect of Reynolds number and angle of attack upon flow field.  $T_w/T_t \approx 0.5$ ;  $M_\infty = 8$ ;  $r_n/D = 0.14$ . L-66-7614



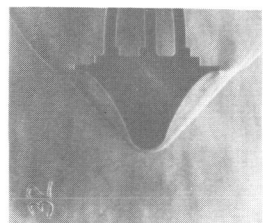
$1.36 \times 10^6$  unsteady



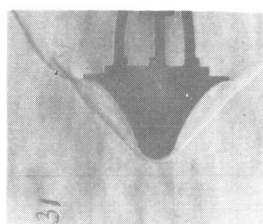
$0.69 \times 10^6$  unsteady



$0.69 \times 10^6$  unsteady

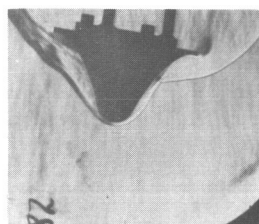


$0.24 \times 10^6$  steady

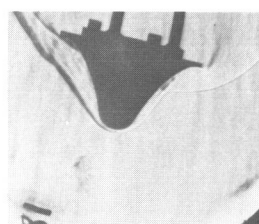


$0.106 \times 10^6$  steady

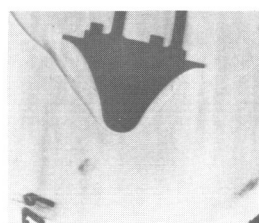
(a)  $\alpha = 0^\circ$ .



$1.36 \times 10^6$  unsteady

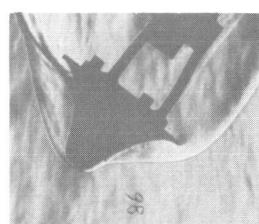


$0.69 \times 10^6$  unsteady

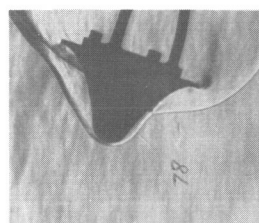


$0.106 \times 10^6$  steady

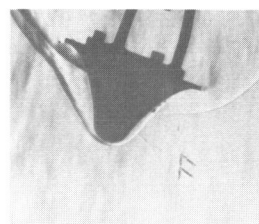
(b)  $\alpha = 8^\circ$ .



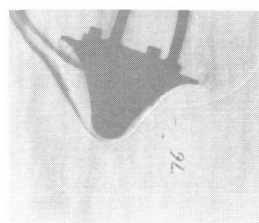
$1.36 \times 10^6$  steady



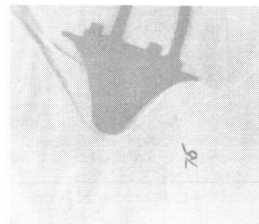
$1.36 \times 10^6$  steady



$0.69 \times 10^6$  steady



$0.24 \times 10^6$  steady



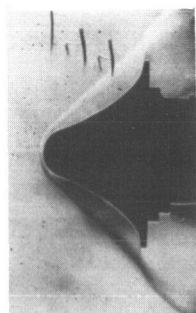
$0.106 \times 10^6$  steady

(c)  $\alpha = 15^\circ$ .

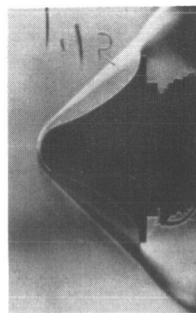
(d)  $\alpha = 31^\circ$ .

Figure 7.- Schlieren photographs of model 4 for the uncooled wall showing effect of Reynolds number and angle of attack upon flow field.  $T_w/T_t \approx 0.5$ ;  $M_\infty = 8$ ;  $r_n/D = 0.134$ . L-66-7615

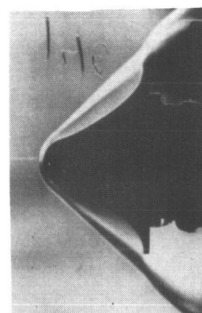
(d) Model 4



$R_{\infty,D}$   $0.18 \times 10^6$  steady

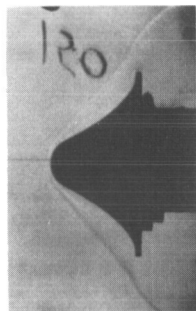


$0.47 \times 10^6$  steady

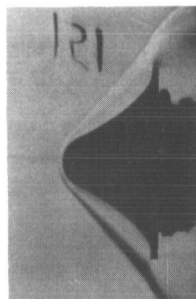


$1.36 \times 10^6$  unsteady

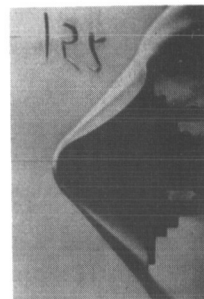
(c) Model 3



$R_{\infty,D}$   $0.18 \times 10^6$  steady

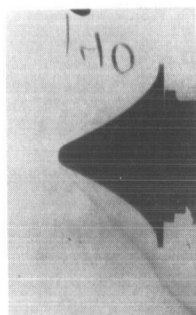


$0.47 \times 10^6$  steady

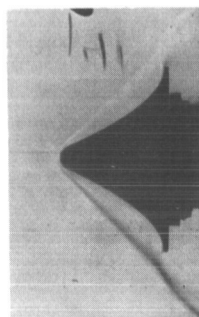


$1.36 \times 10^6$  unsteady

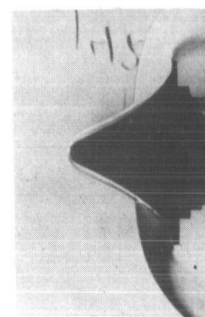
(b) Model 2



$R_{\infty,D}$   $0.18 \times 10^6$  unsteady

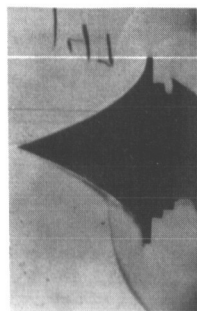


$0.47 \times 10^6$  unsteady

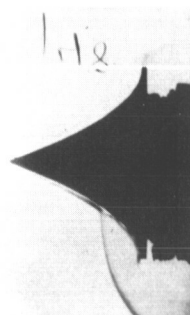


$1.36 \times 10^6$  steady

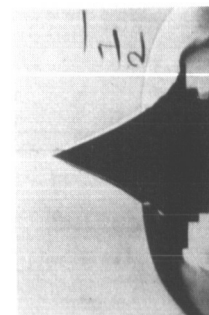
(a) Model 1



$R_{\infty,D}$   $0.18 \times 10^6$  unsteady



$0.47 \times 10^6$  steady



$1.36 \times 10^6$  steady

Figure 8.- Schlieren photographs of models 1 to 4 showing effect of Reynolds number upon flow field.  $\alpha = 0^\circ$ ;  $T_w/T_t \approx 0.2$ . L-66-7616

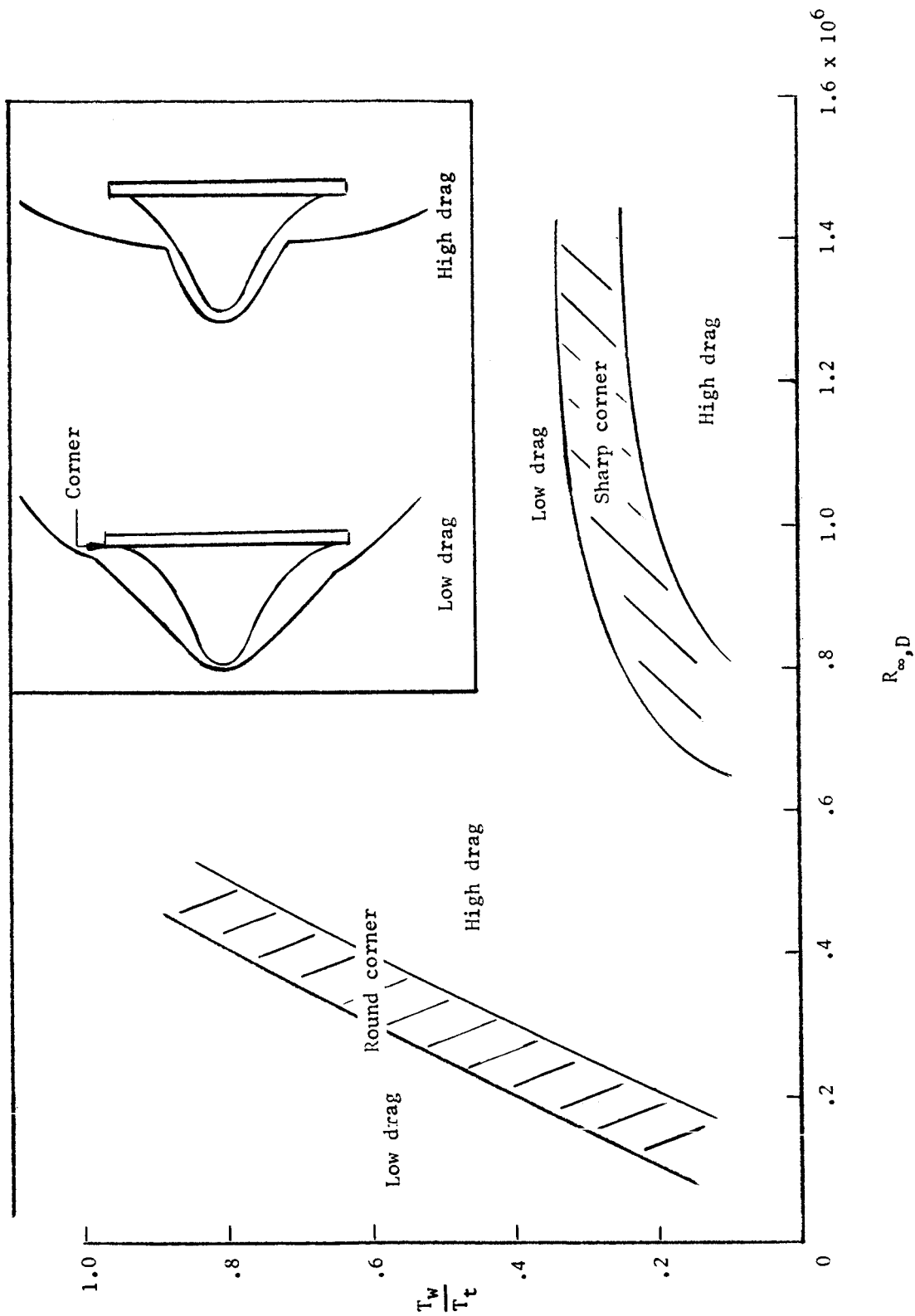


Figure 9.- Effect of wall temperature and corner radius on shock shape for model 2.  $\alpha = 0^\circ$ .

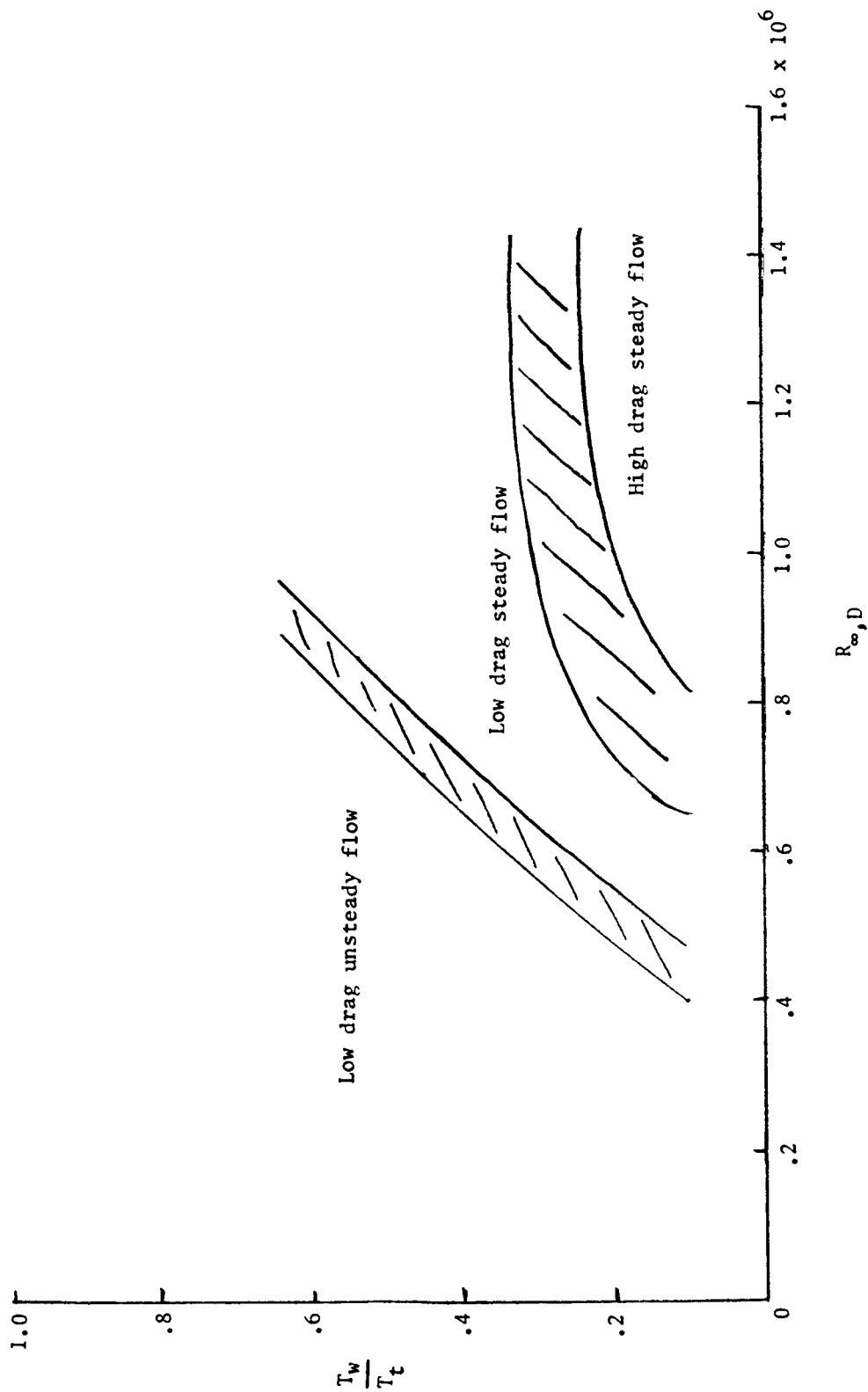
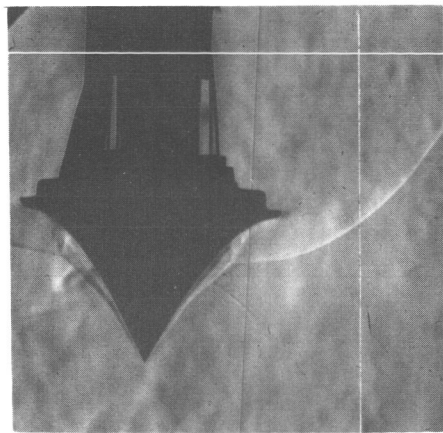
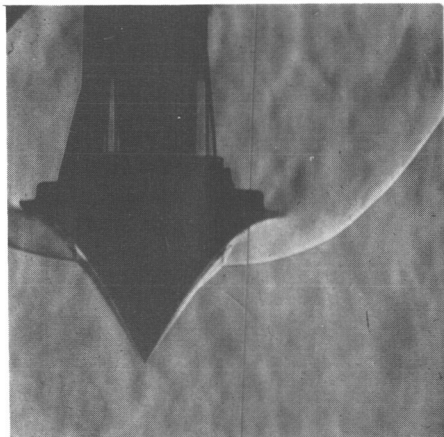


Figure 10.- Effect of wall temperature and Reynolds number on flow stability for model 2, sharp corner.  $\alpha = 0^\circ$ .



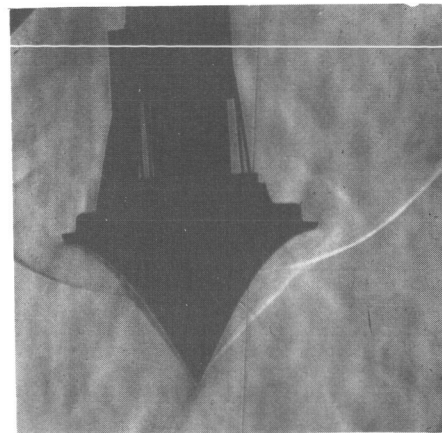


$$R_{\infty,D} = .2 \times 10^6, T_w/T_t = .54$$

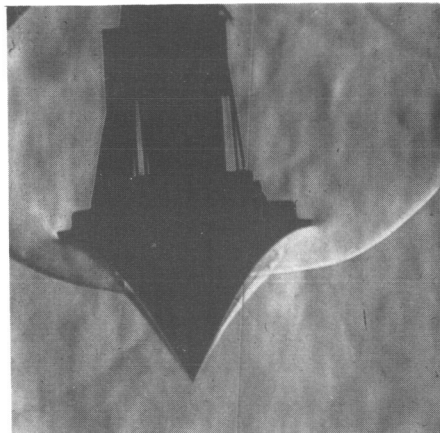


$$R_{\infty,D} = .5 \times 10^6, T_w/T_t = .60$$

(a)  $\alpha = 0^\circ$ .

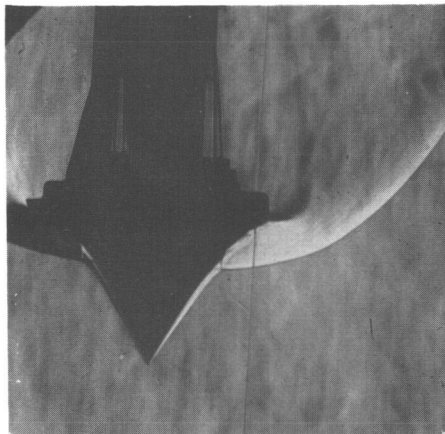


$$R_{\infty,D} = .2 \times 10^6, T_w/T_t = .52$$

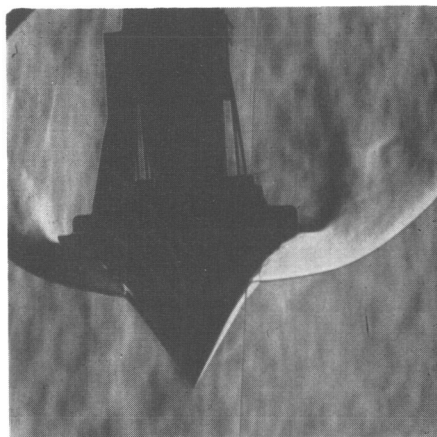


$$R_{\infty,D} = .5 \times 10^6, T_w/T_t = .46$$

(b)  $\alpha = 5^\circ$ .



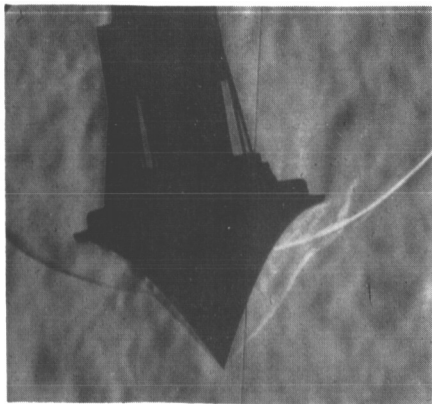
$$R_{\infty,D} = 1.5 \times 10^6, T_w/T_t = .72$$



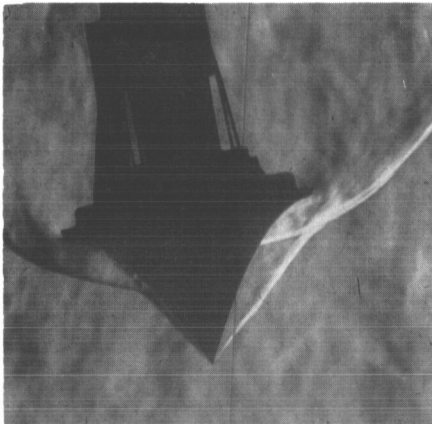
$$R_{\infty,D} = 1.5 \times 10^6, T_w/T_t = .72$$

Figure 11.- Schlieren photographs of model 5.  $r_n/D = 0$ ;  $M_\infty = 8$ .

L-66-7617

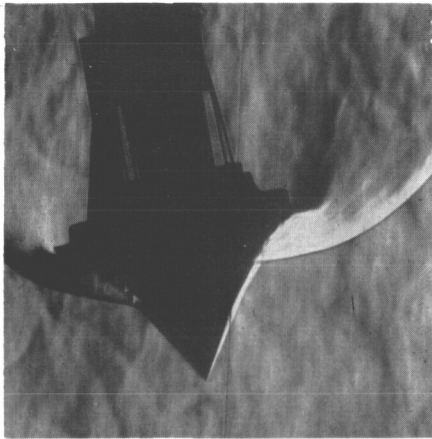


$$R_{\infty,D} = .2 \times 10^6, T_w/T_t = .52$$

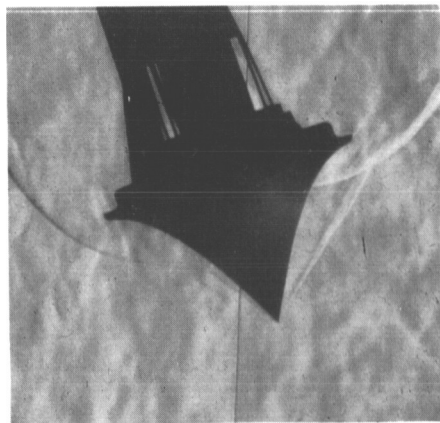


$$R_{\infty,D} = .5 \times 10^6, T_w/T_t = .56$$

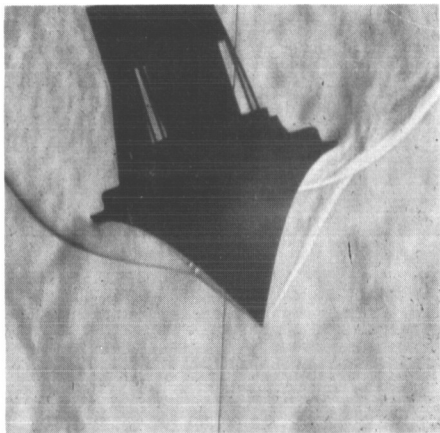
(c)  $\alpha = 12^\circ$ .



$$R_{\infty,D} = 1.5 \times 10^6, T_w/T_t = .72$$

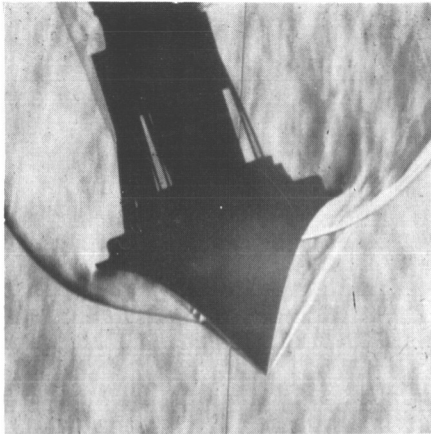


$$R_{\infty,D} = .2 \times 10^6, T_w/T_t = .50$$



$$R_{\infty,D} = .5 \times 10^6, T_w/T_t = .53$$

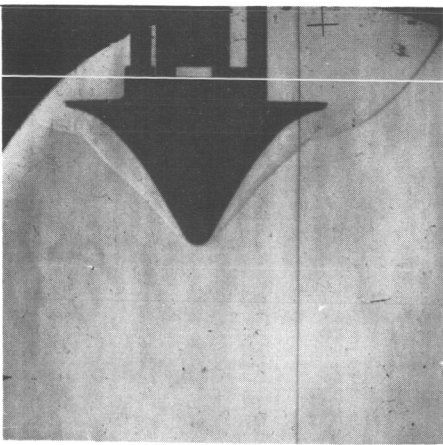
(d)  $\alpha = 20^\circ$ .



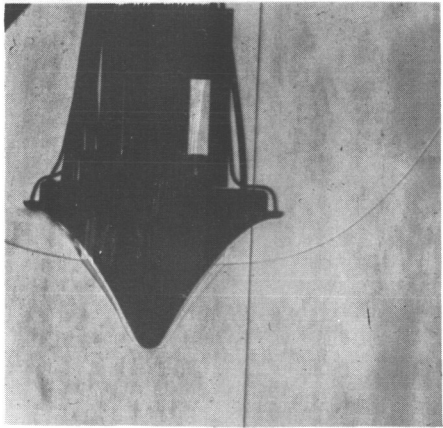
$$R_{\infty,D} = 1.5 \times 10^6, T_w/T_t = .65$$

Figure 11.- Concluded.

L-66-7618

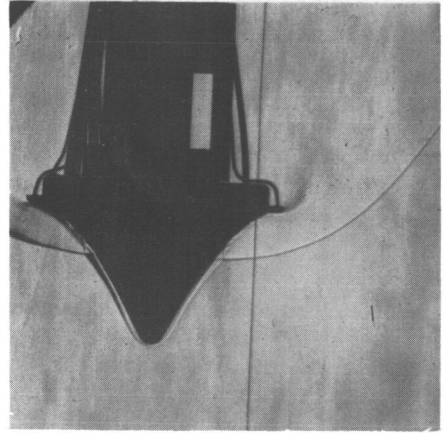


$$R_{\infty, D} = .2 \times 10^6, T_w/T_t = .50$$

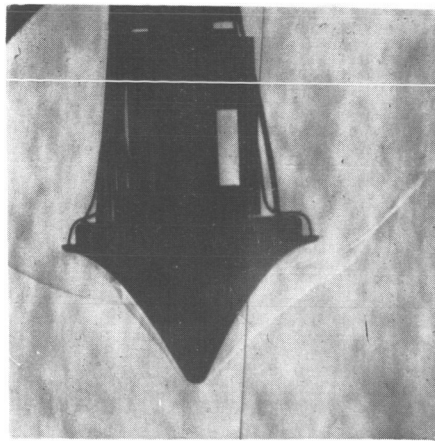


$$R_{\infty, D} = .5 \times 10^6, T_w/T_t = .52$$

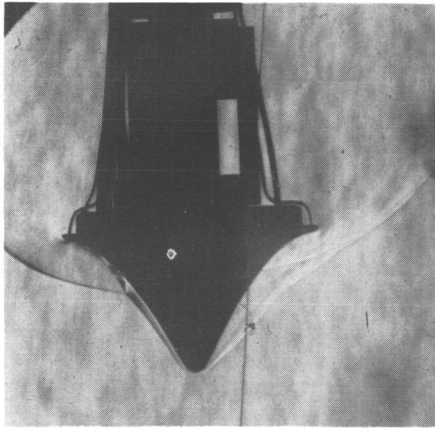
(a)  $\alpha = 0^\circ$ .



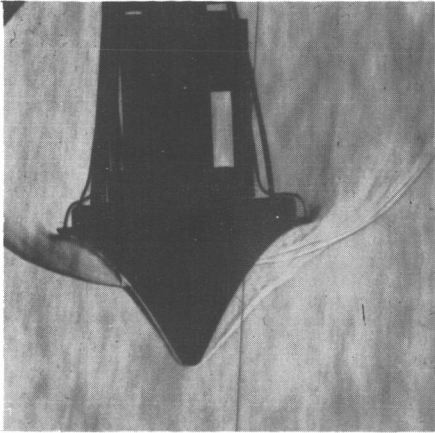
$$R_{\infty, D} = 1.5 \times 10^6, T_w/T_t = .66$$



$$R_{\infty, D} = .2 \times 10^6, T_w/T_t = .49$$



$$R_{\infty, D} = .5 \times 10^6, T_w/T_t = .54$$

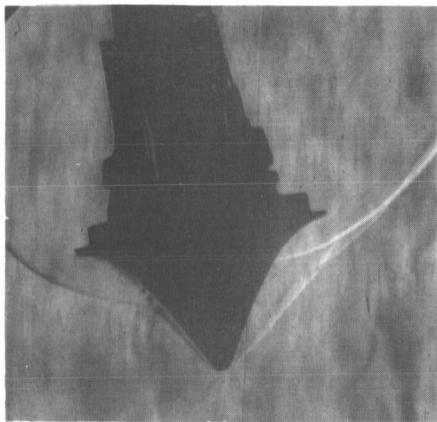


$$R_{\infty, D} = 1.5 \times 10^6, T_w/T_t = .66$$

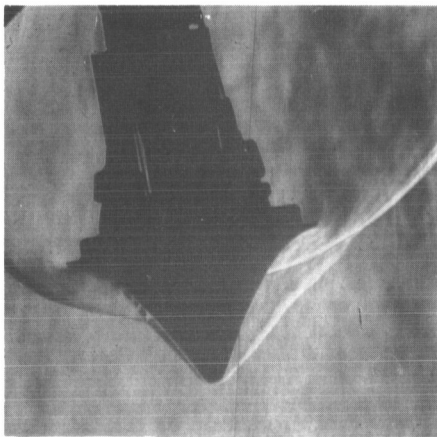
(b)  $\alpha = 5^\circ$ .

Figure 12.- Schlieren photographs of model 6.  $r_n/D = 0.05$ ;  $M_\infty = 8$ .

L-66-7619

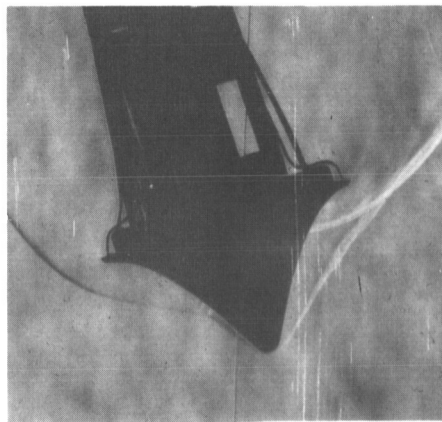


$$R_{\infty,D} = .2 \times 10^6, T_w/T_t = .42$$

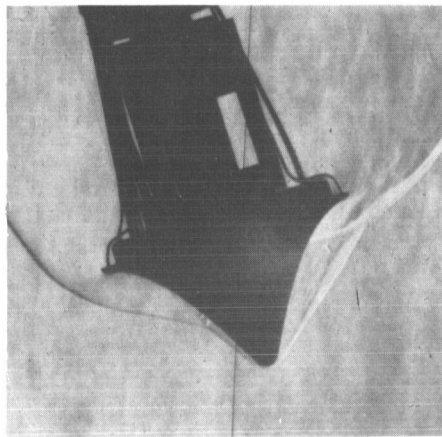


$$R_{\infty,D} = .5 \times 10^6, T_w/T_t = .42$$

(c)  $\alpha = 12^\circ$

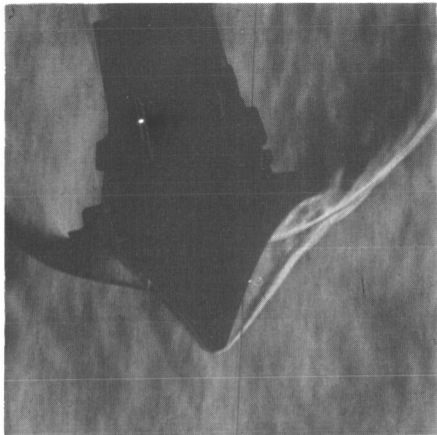


$$R_{\infty,D} = .2 \times 10^6, T_w/T_t = .49$$

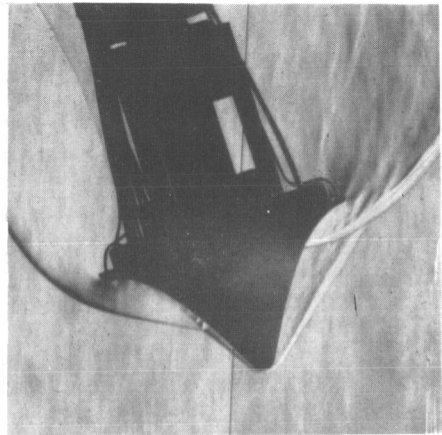


$$R_{\infty,D} = .5 \times 10^6, T_w/T_t = .42$$

(d)  $\alpha = 20^\circ$



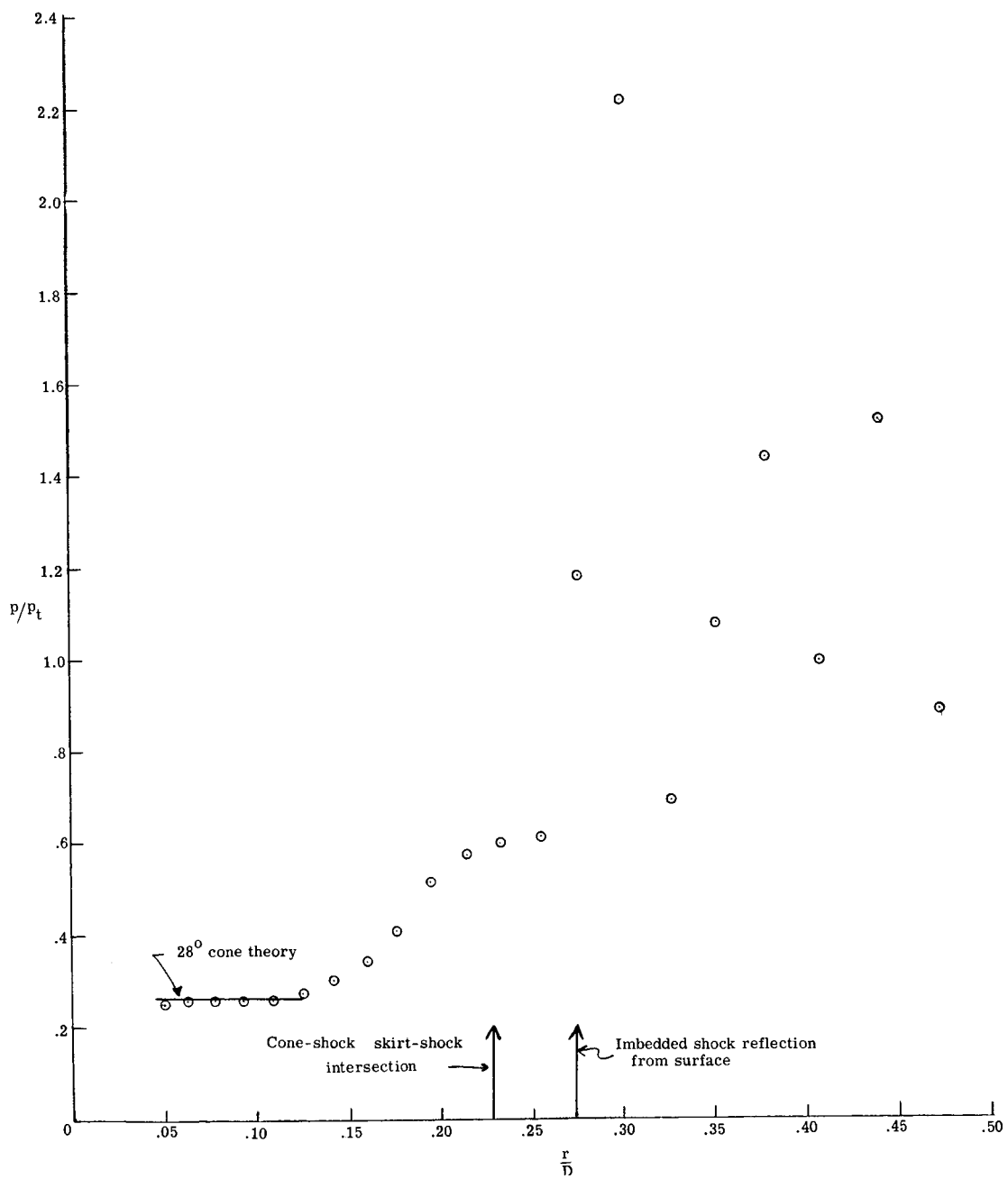
$$R_{\infty,D} = 1.5 \times 10^6, T_w/T_t = .45$$



$$R_{\infty,D} = 1.5 \times 10^6, T_w/T_t = .54$$

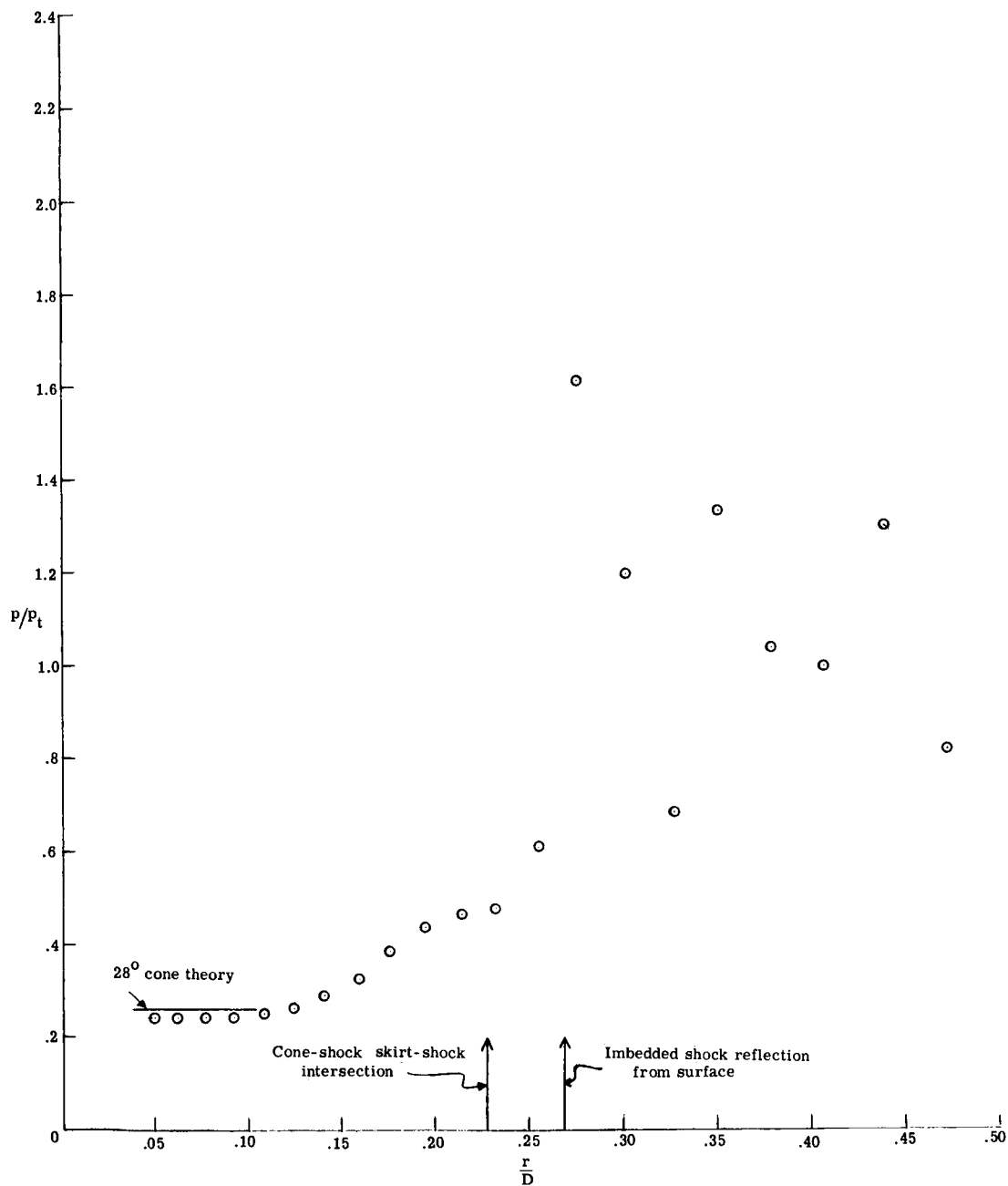
Figure 12.- Concluded.

L-66-7620



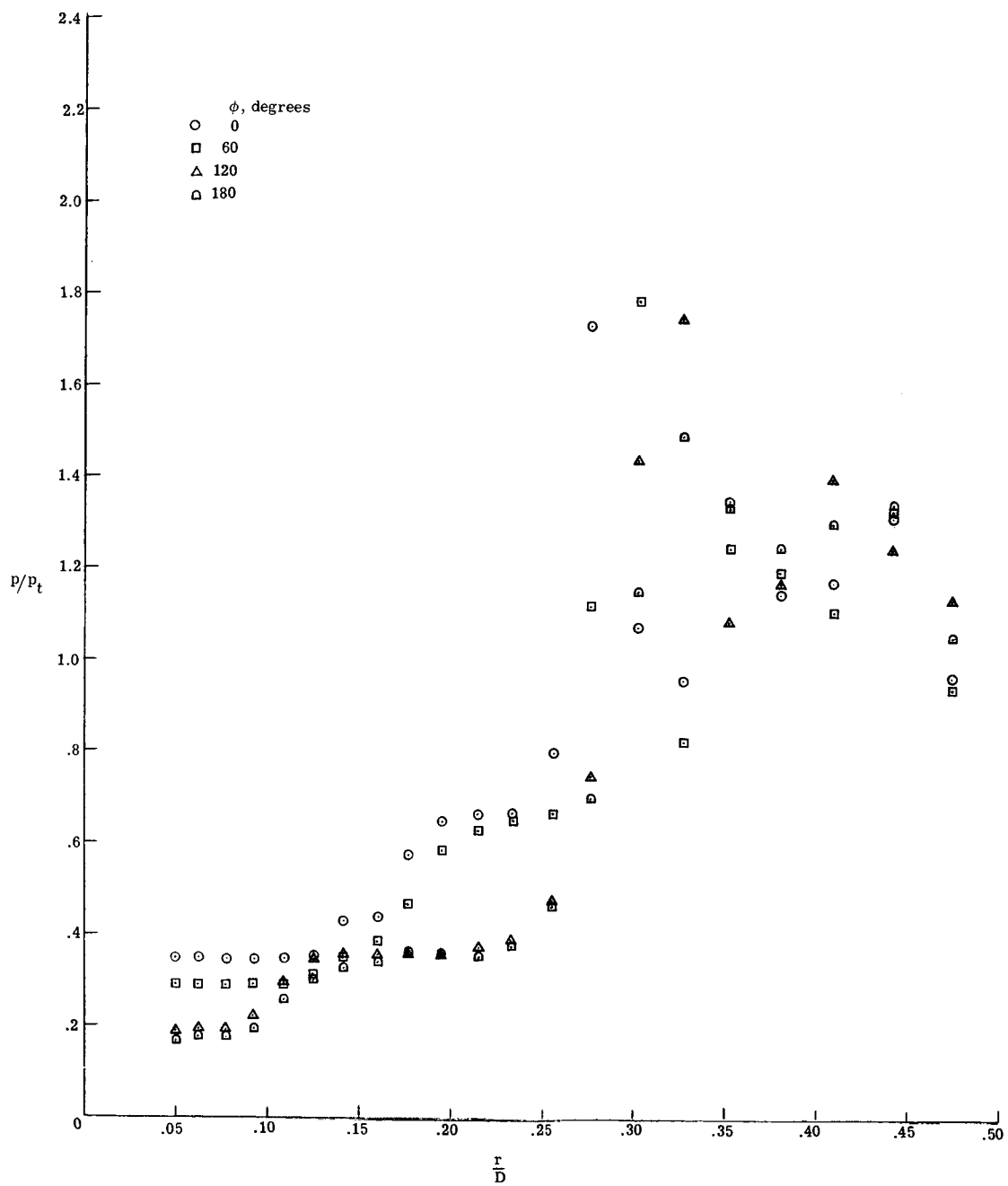
(a)  $\alpha = 0^\circ$ ;  $R_{\infty, D} = 0.5 \times 10^6$ .

Figure 13.- Pressure distribution for model 5.  $r_n/D = 0$ .



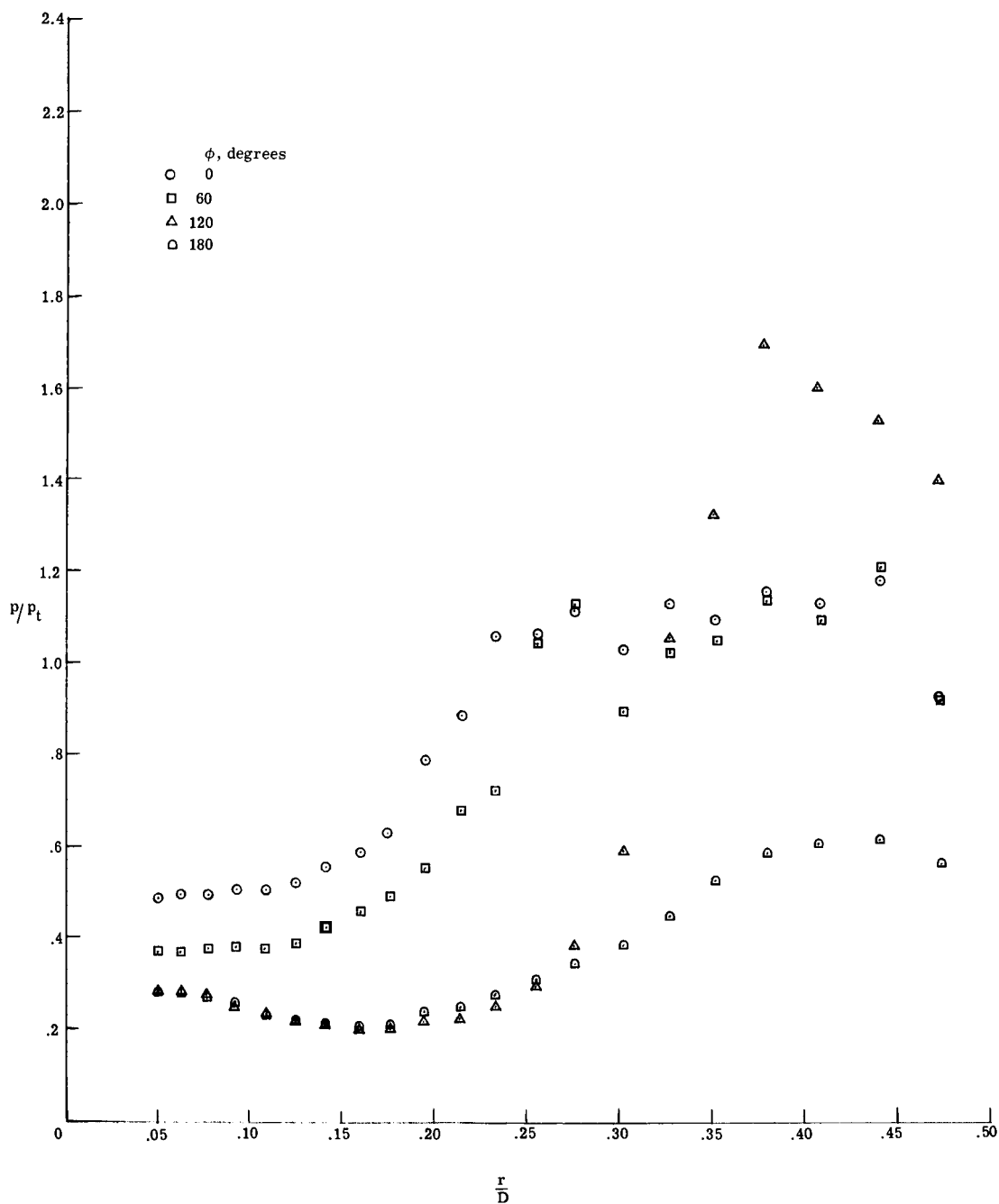
(b)  $\alpha = 0^\circ$ ;  $R_{\infty, D} = 1.4 \times 10^6$ .

Figure 13.- Continued.



(c)  $\alpha = 5^\circ$ ;  $R_{\infty, D} = 0.5 \times 10^6$ .

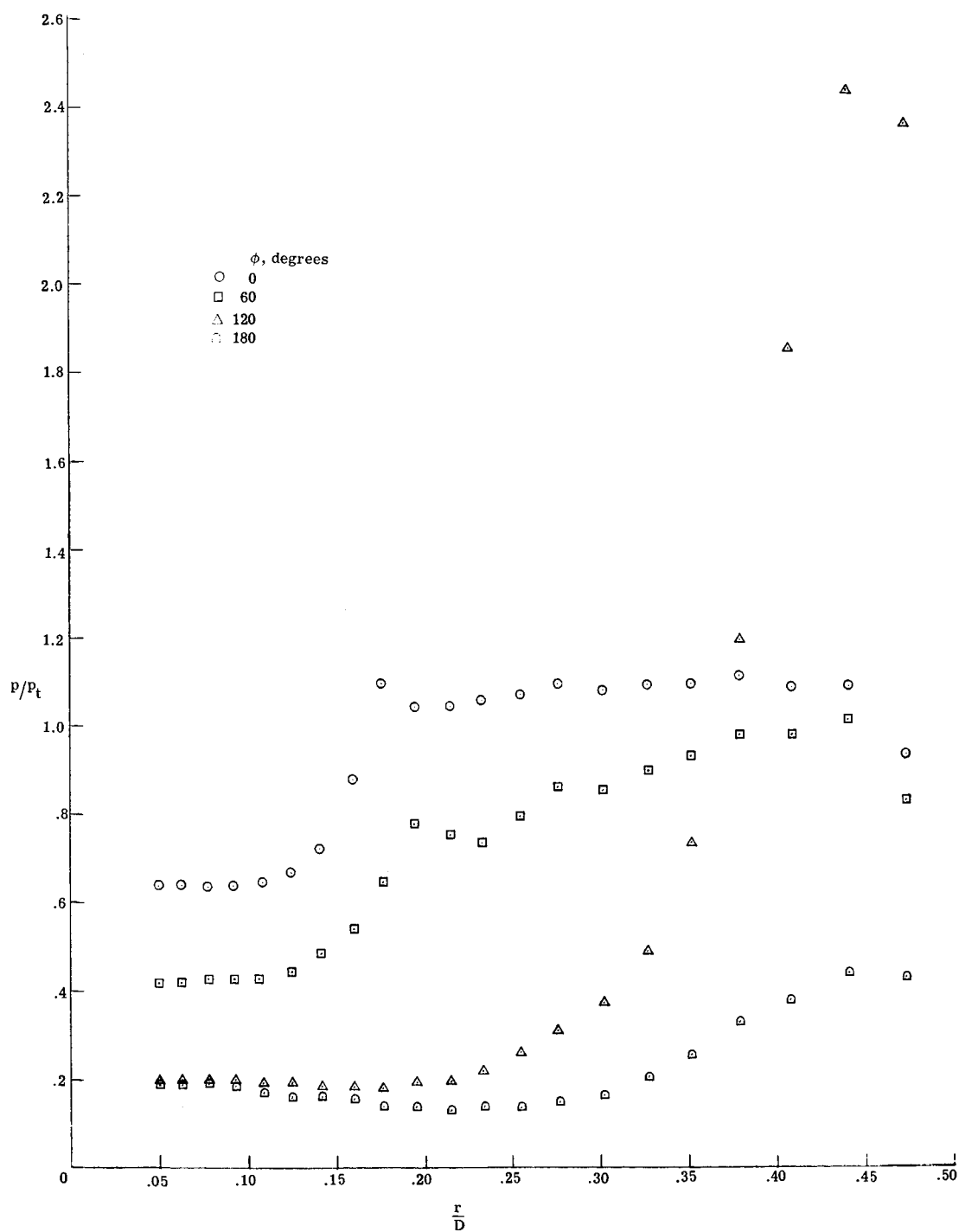
Figure 13.- Continued.



(d)  $\alpha = 12^\circ$ ;  $R_{\infty, D} = 0.5 \times 10^6$ .

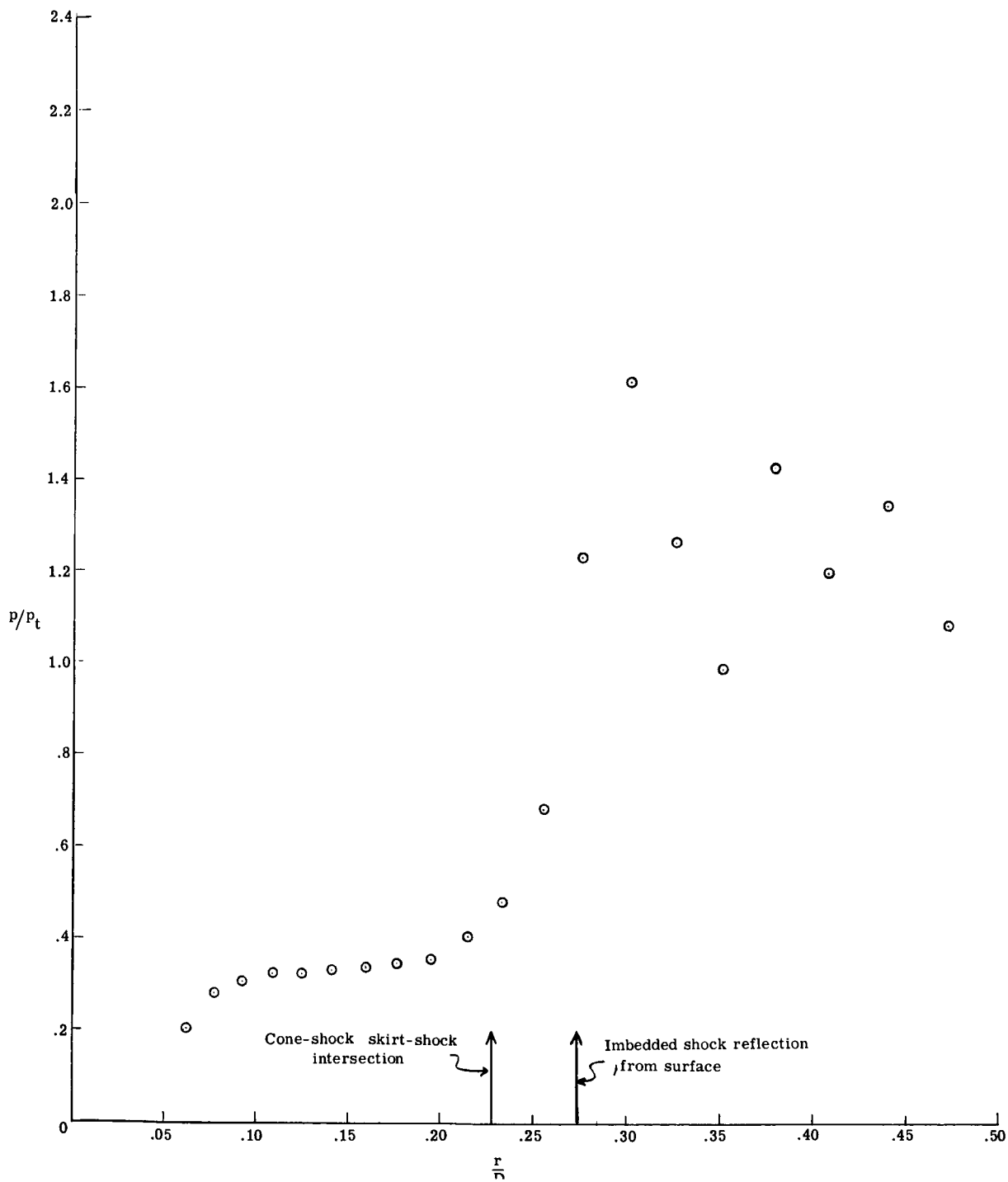
Figure 13.- Continued.





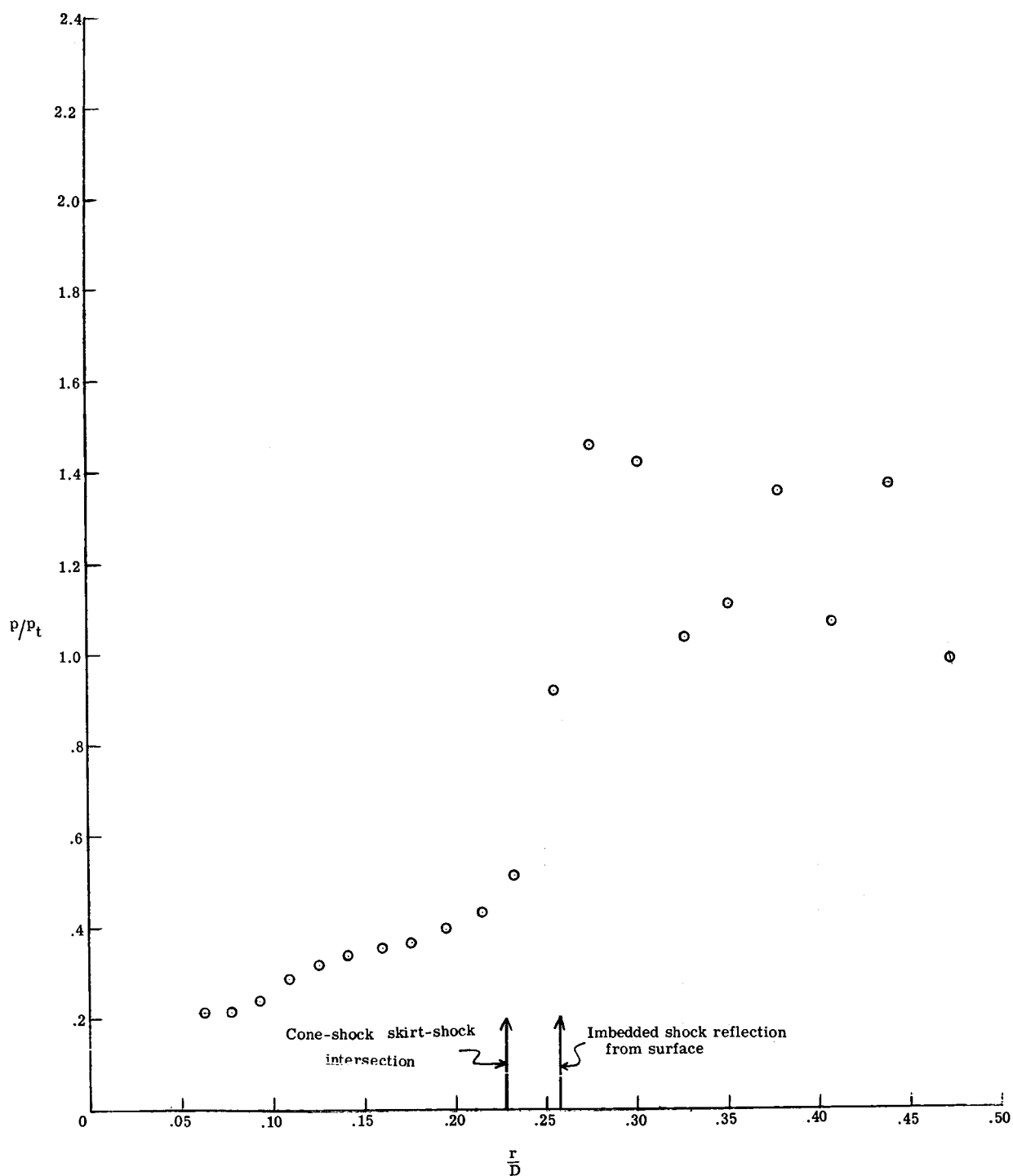
(e)  $\alpha = 20^\circ$ ;  $R_{\infty, D} = 0.5 \times 10^6$ .

Figure 13.- Concluded.



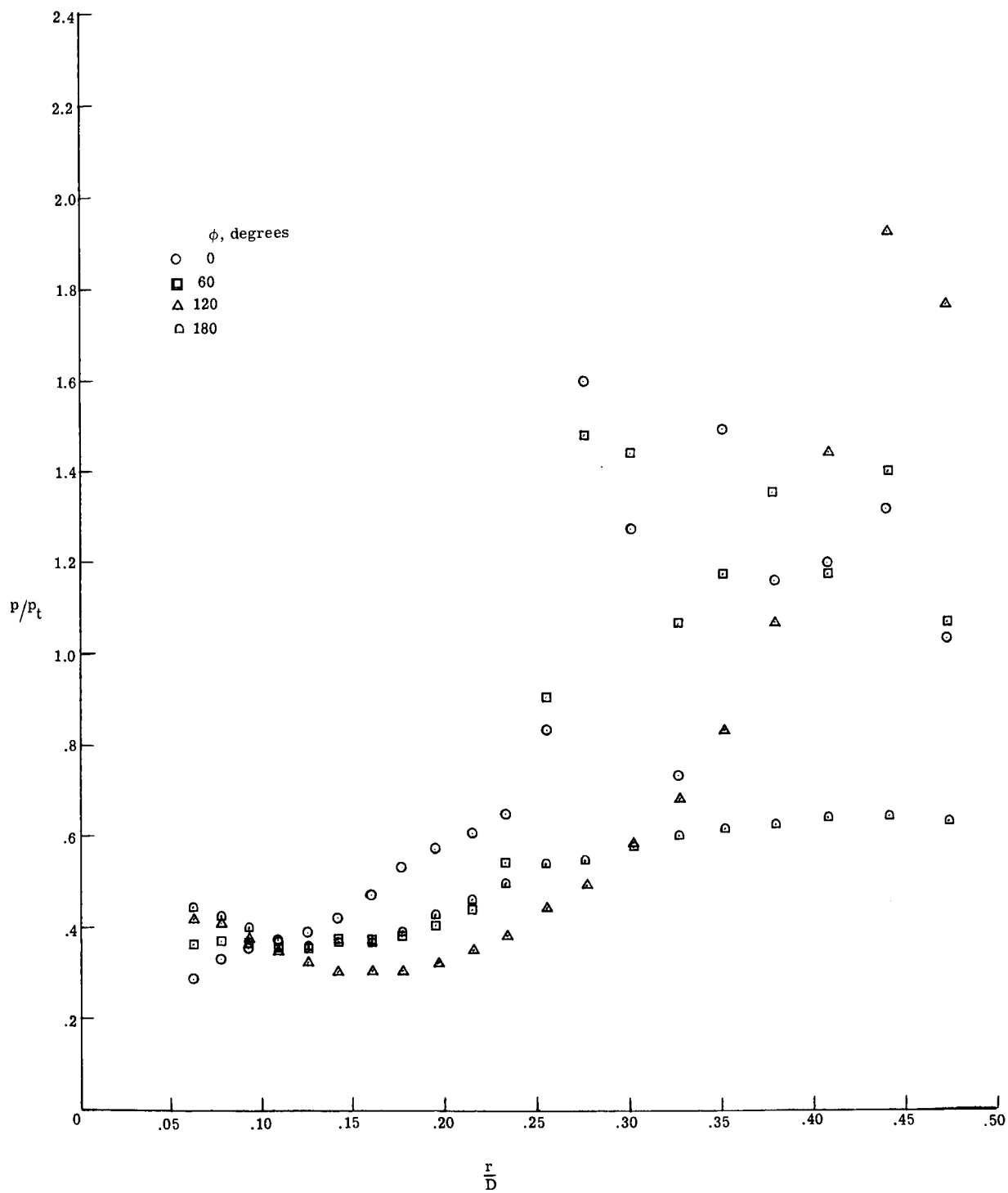
(a)  $\alpha = 0^\circ$ ;  $R_{\infty, D} = 0.5 \times 10^6$ .

Figure 14.- Pressure distribution for model 6.  $r_n/D = 0.05$ .



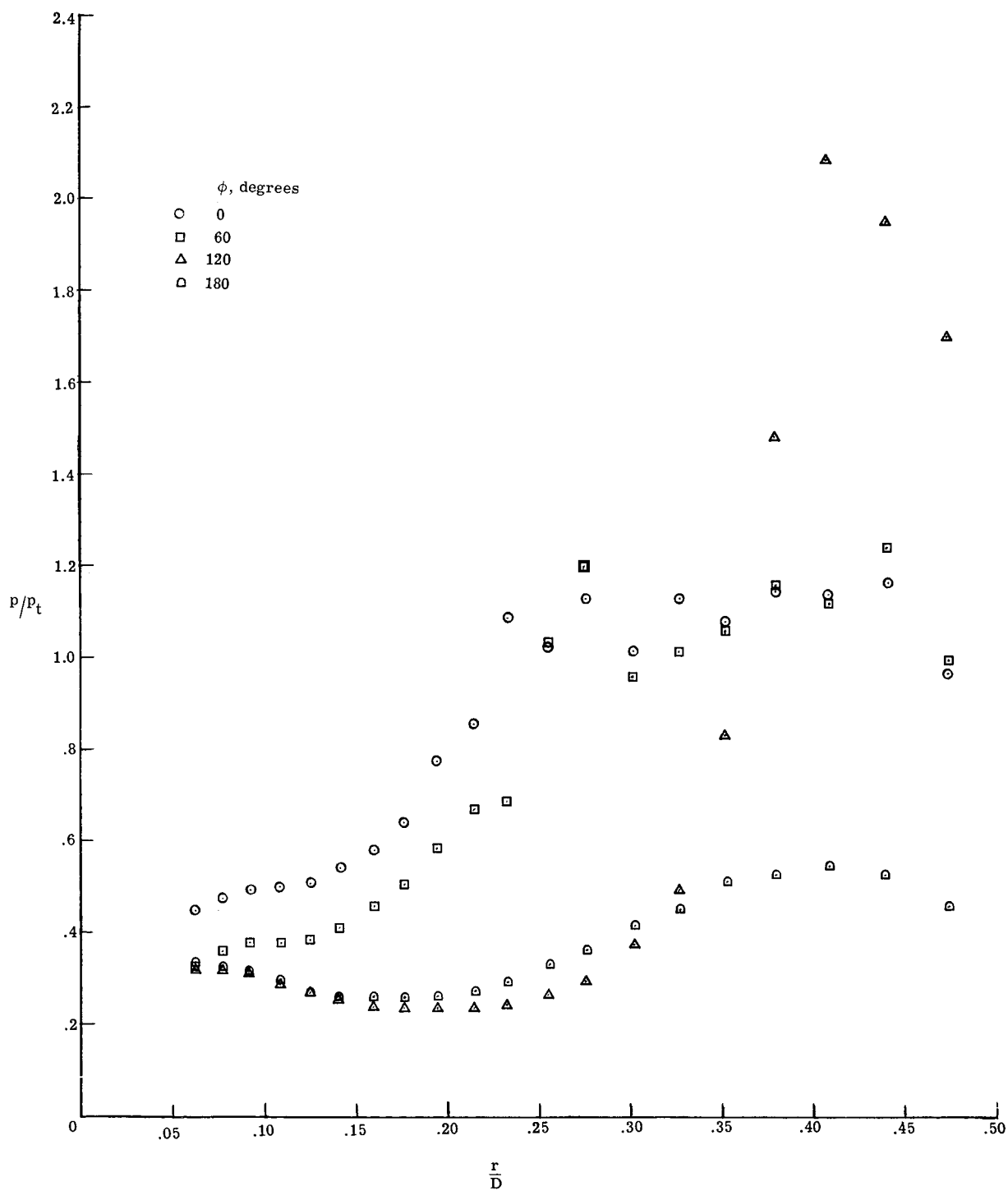
(b)  $\alpha = 0^\circ$ ;  $R_{\infty, D} = 1.4 \times 10^6$ .

Figure 14.- Continued.



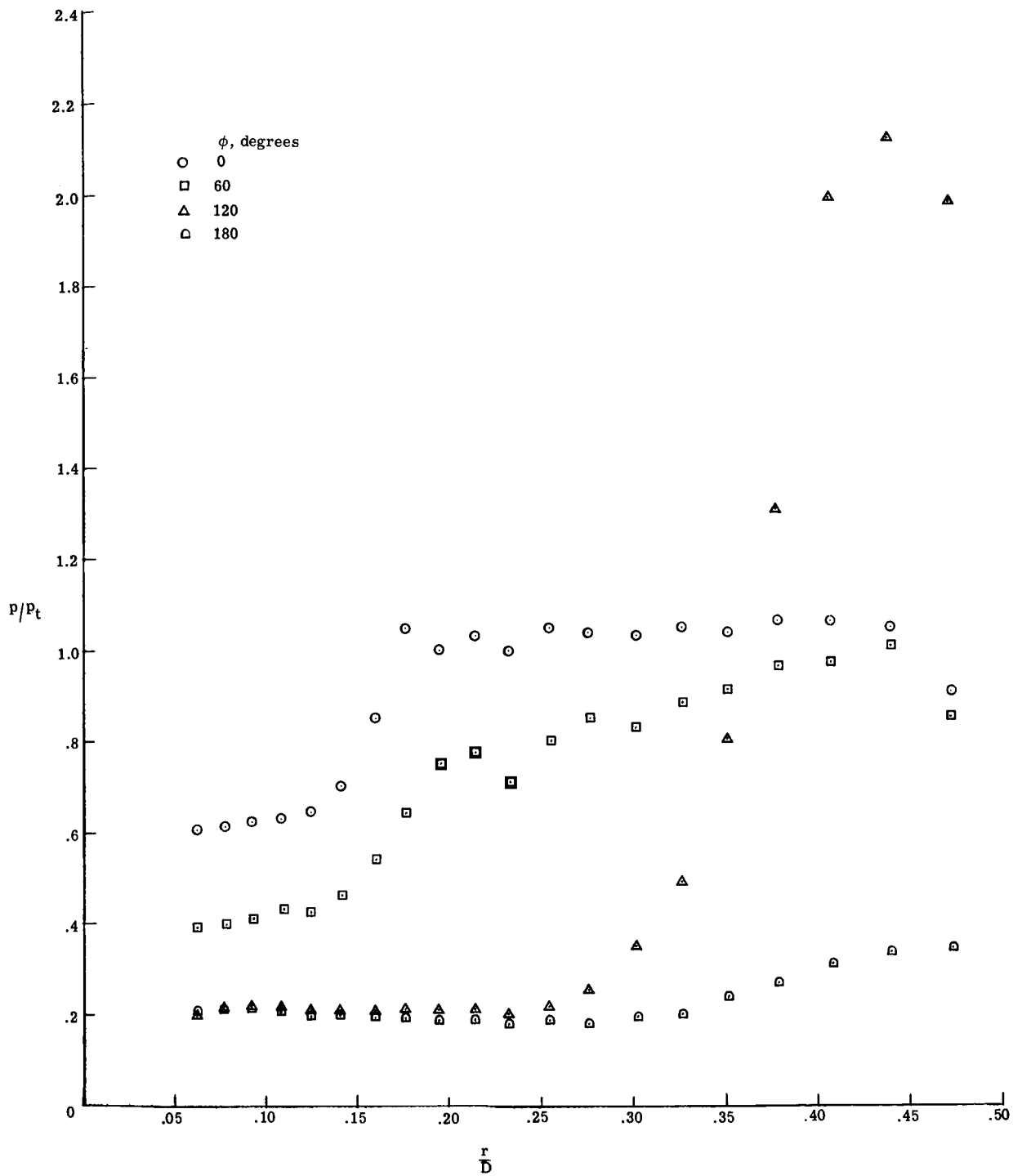
(c)  $\alpha = 5^\circ$ ;  $R_{\infty, D} = 0.5 \times 10^6$ .

Figure 14.- Continued.



(d)  $\alpha = 12^\circ$ ;  $R_{\infty, D} = 0.5 \times 10^6$ .

Figure 14.- Continued.



(e)  $\alpha = 20^\circ$ ;  $R_{\infty, D} = 0.5 \times 10^6$ .

Figure 14.- Concluded.

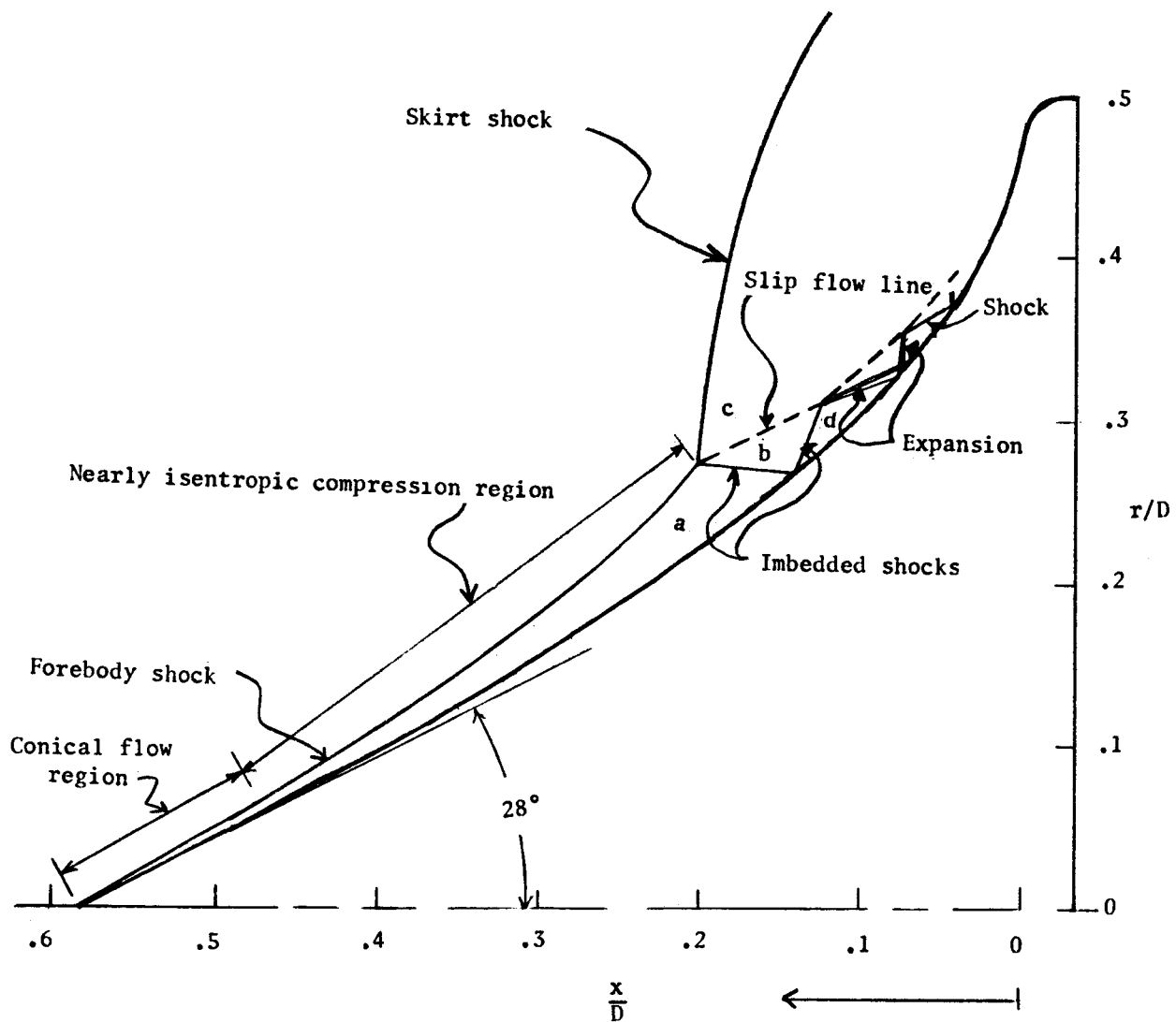


Figure 15.- Sketch of flow field from figure 11 for model 5  $r_n/D = 0$ ,  $\alpha = 0^\circ$ ;  $D = 0.5 \times 10^6$ .

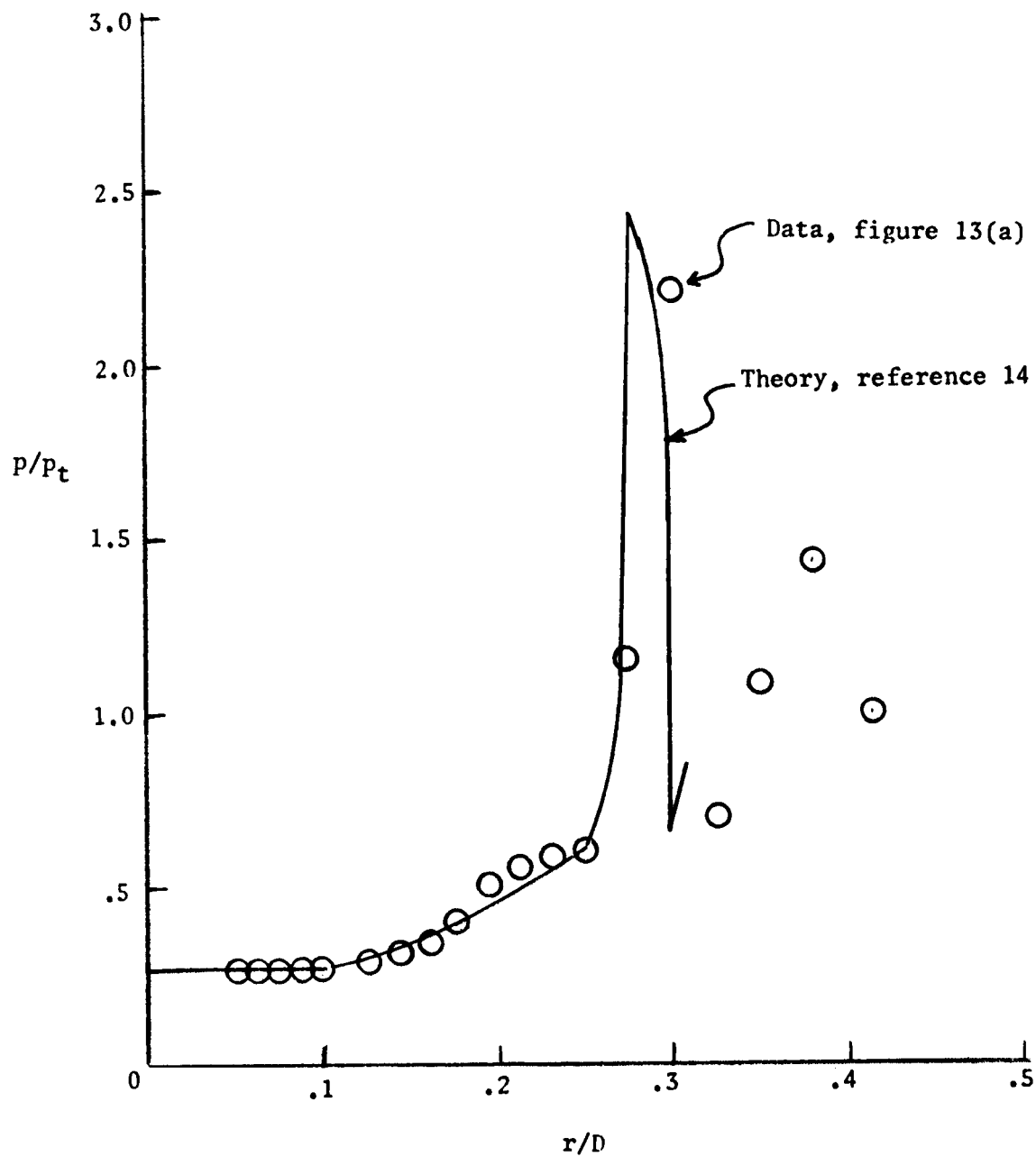


Figure 16.- Comparison of predicted and measured pressure distributions for model 5 ( $r_n/D = 0$ ).  $\alpha = 0^\circ$ ;  $R_{\infty,D} = 0.5 \times 10^6$ .



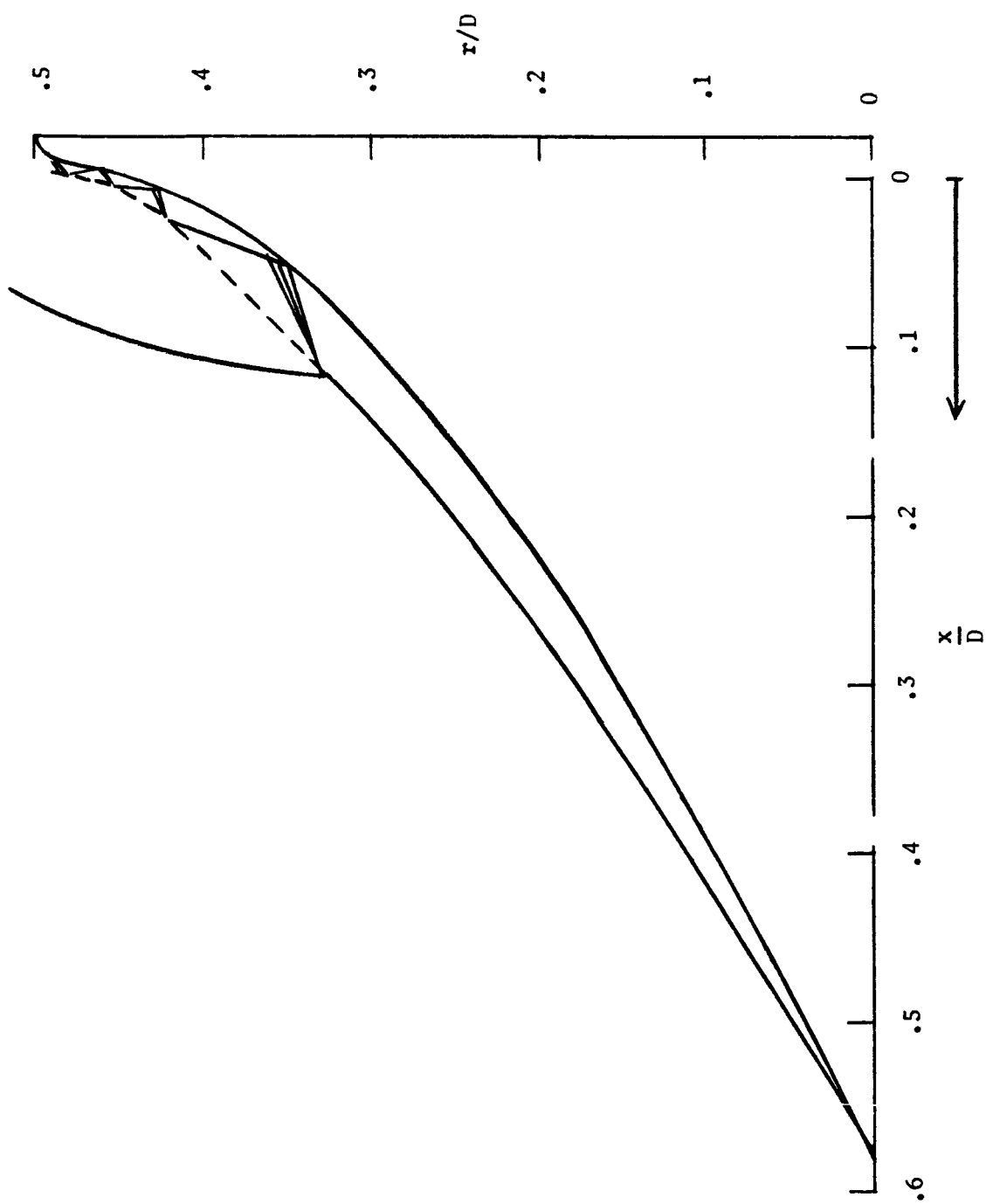


Figure 17.- Sketch of flow field calculated in reference 14 for Martian entry, model 5 ( $r_n/D = 0$ ).  $\rho_s/\rho_\infty = 16.7$ ;  $\alpha = 0^\circ$ .

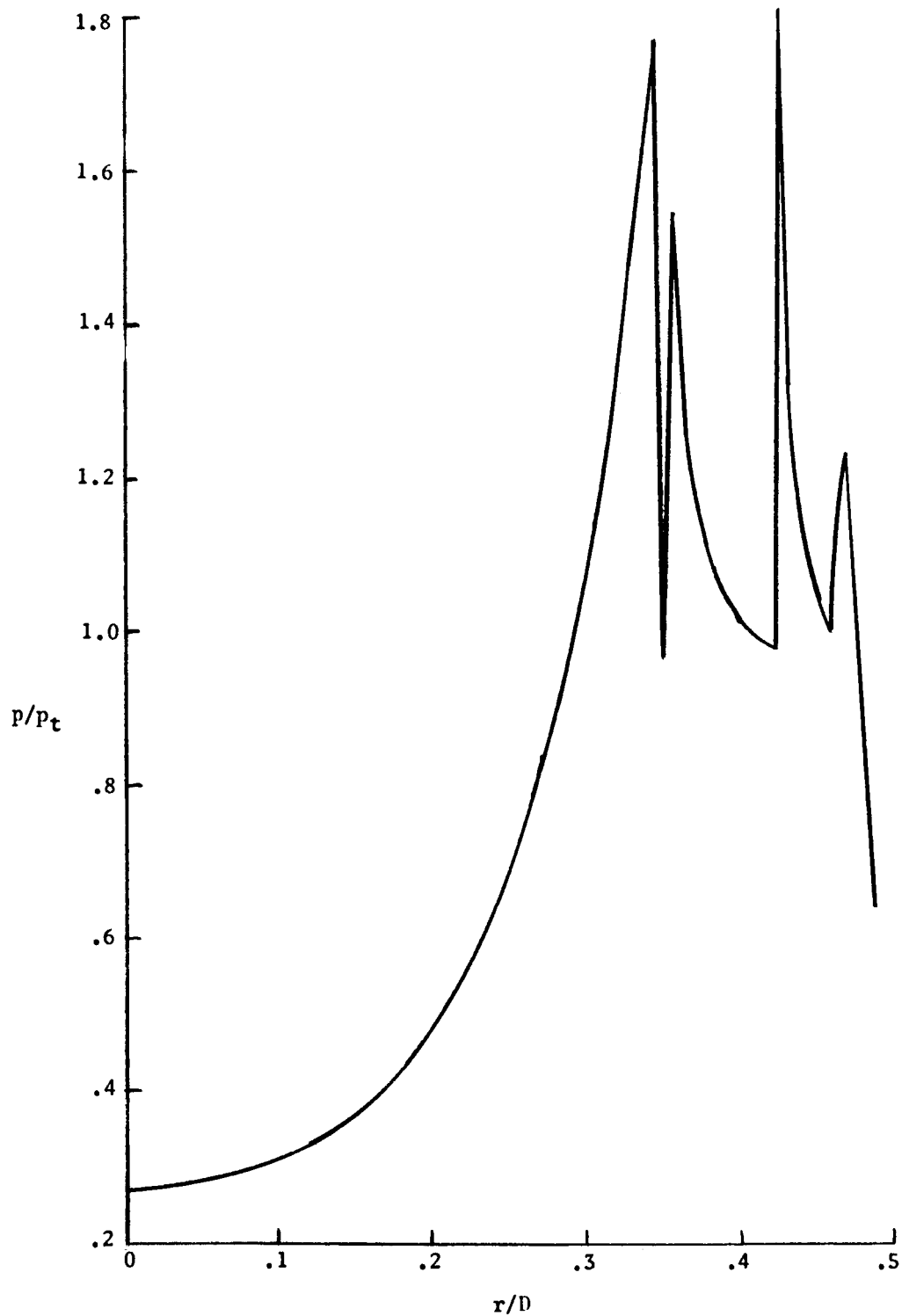
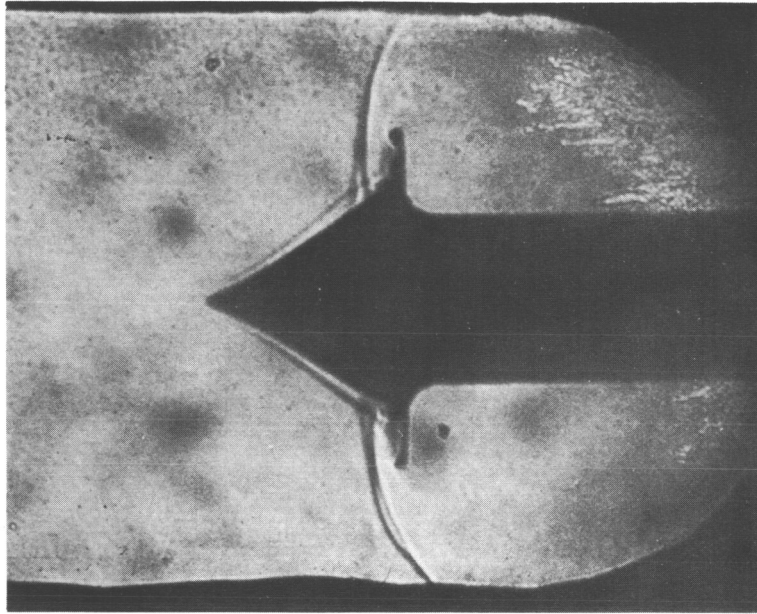
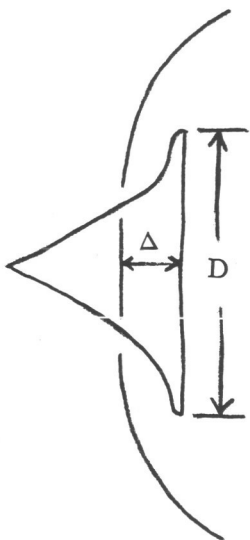


Figure 18.- Pressure distribution calculated in reference 14 for Martian entry, model 5 ( $r_n/D = 0$ ).  $\rho_s/p_\infty = 16.7$ ;  $\alpha = 0^\circ$ .

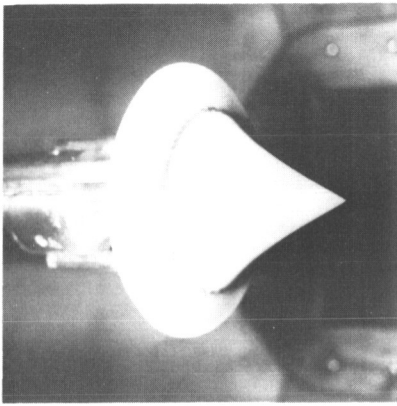


Shadowgraph taken in  $\text{CF}_4$  facility

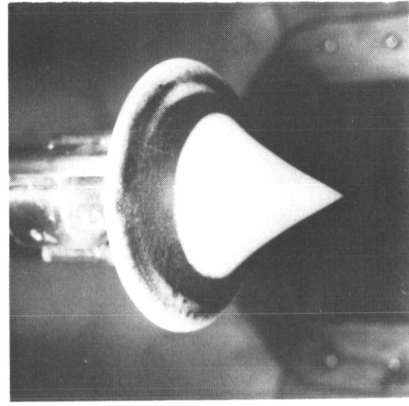


	Test results		Theory	
	Air	$\text{CF}_4$	Air	Martian entry
$M_\infty$	8	8	8	20
$\rho_s/\rho_\infty$	5.6	10	5.6	16.7
$\Delta/D$	0.21	0.14	0.24	0.14

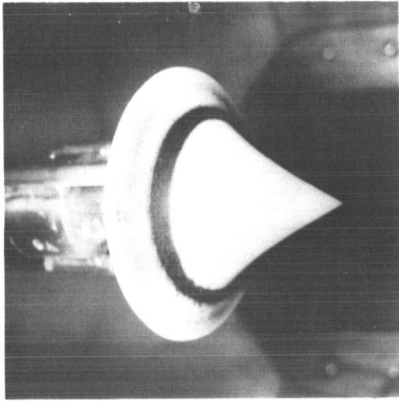
Figure 19.- Comparison of calculated and measured shock standoff distances for model 5 ( $r_n/D = 0$ ) at several values of  $\rho_s/\rho_\infty$ . L-66-7621



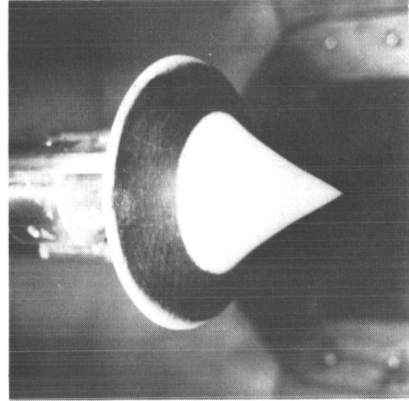
1



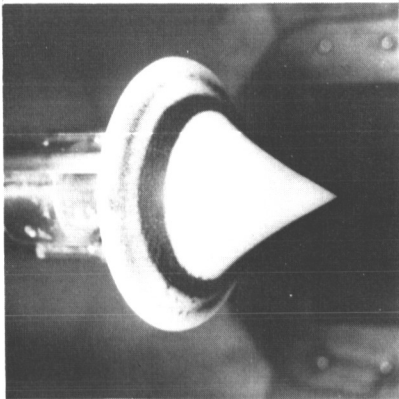
4



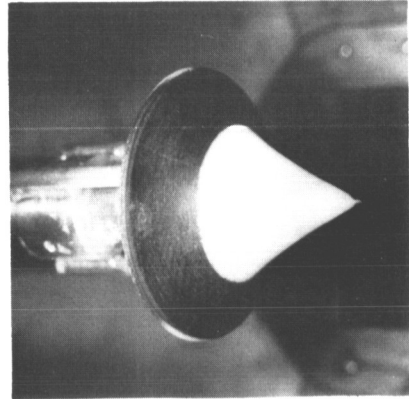
2



5



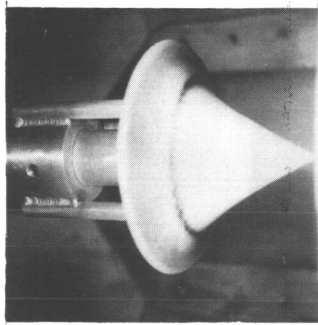
3



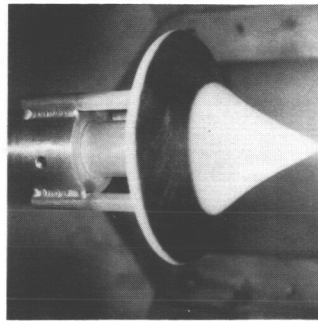
6

Figure 20.- Phase-change patterns for model 5 ( $r_n/D = 0$ ).  $\alpha = 0^\circ$ ;  $R_{\infty,D} = 0.2 \times 10^6$ .

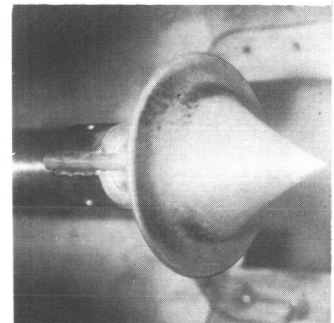
L-66-7622



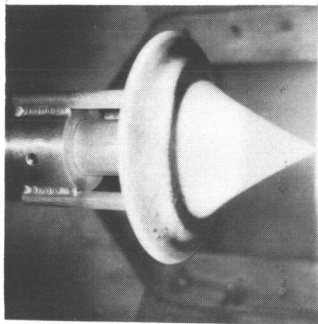
1



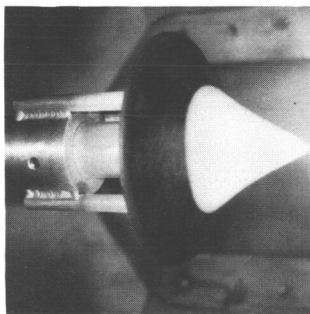
4



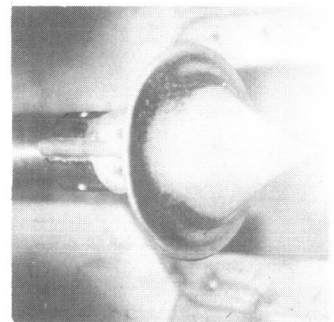
1



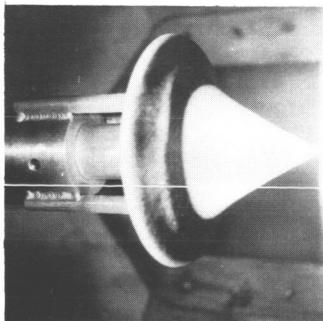
2



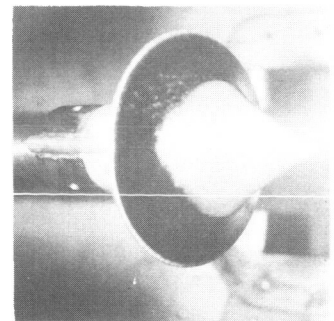
5



2



3



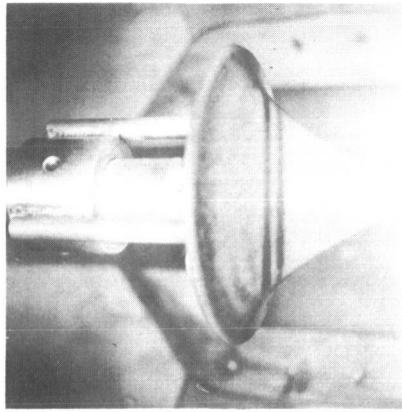
3

(a) Windward portion.

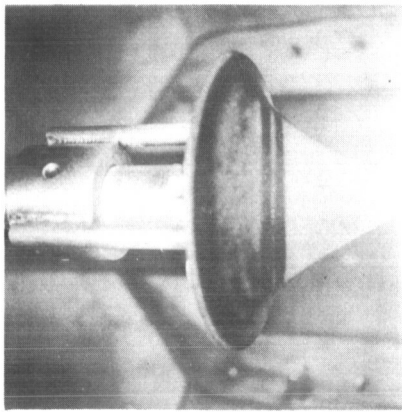
(b) Leeward portion.

Figure 21.- Phase-change patterns for model 5 ( $r_n/D = 0$ ).  $\alpha = 5^\circ$ ;  $R_{\infty,D} = 0.2 \times 10^6$ .

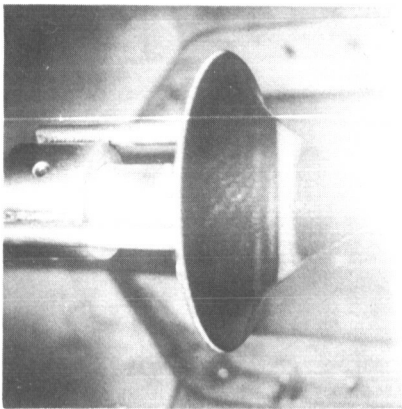
L-66-7623



1



2



3

Figure 22.- Phase-change patterns for model 5 ( $r_n/D = 0$ ).  $\alpha = 12^\circ$ ;  $R_{\infty,D} = 0.2 \times 10^6$ ; windward portion.

L-66-7624

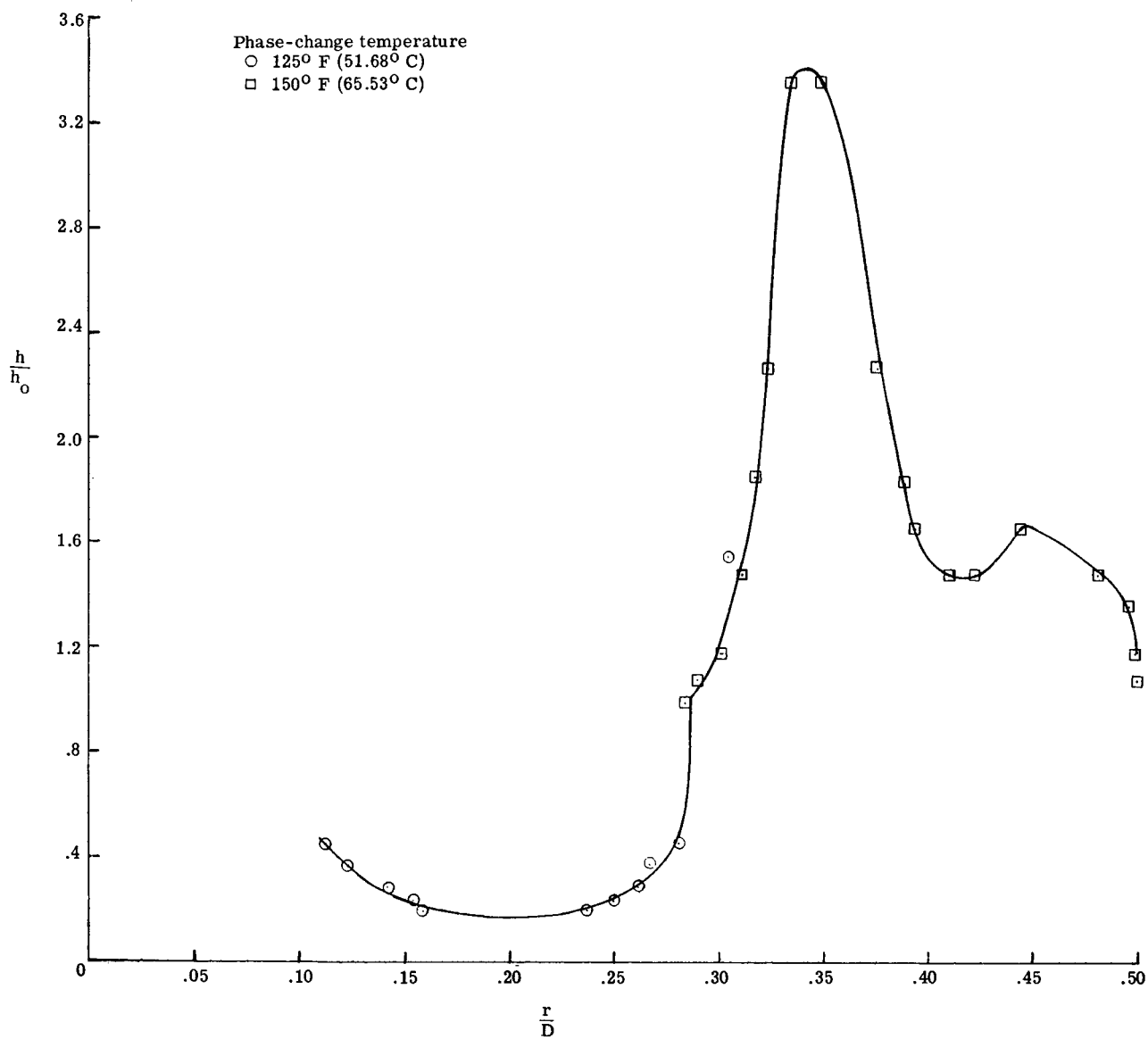


Figure 23.- Heat-transfer distribution for model 5 ( $r_{n/D} = 0$ ).  $\alpha = 0^\circ$ ;  $R_{\infty, D} = 0.2 \times 10^6$ .

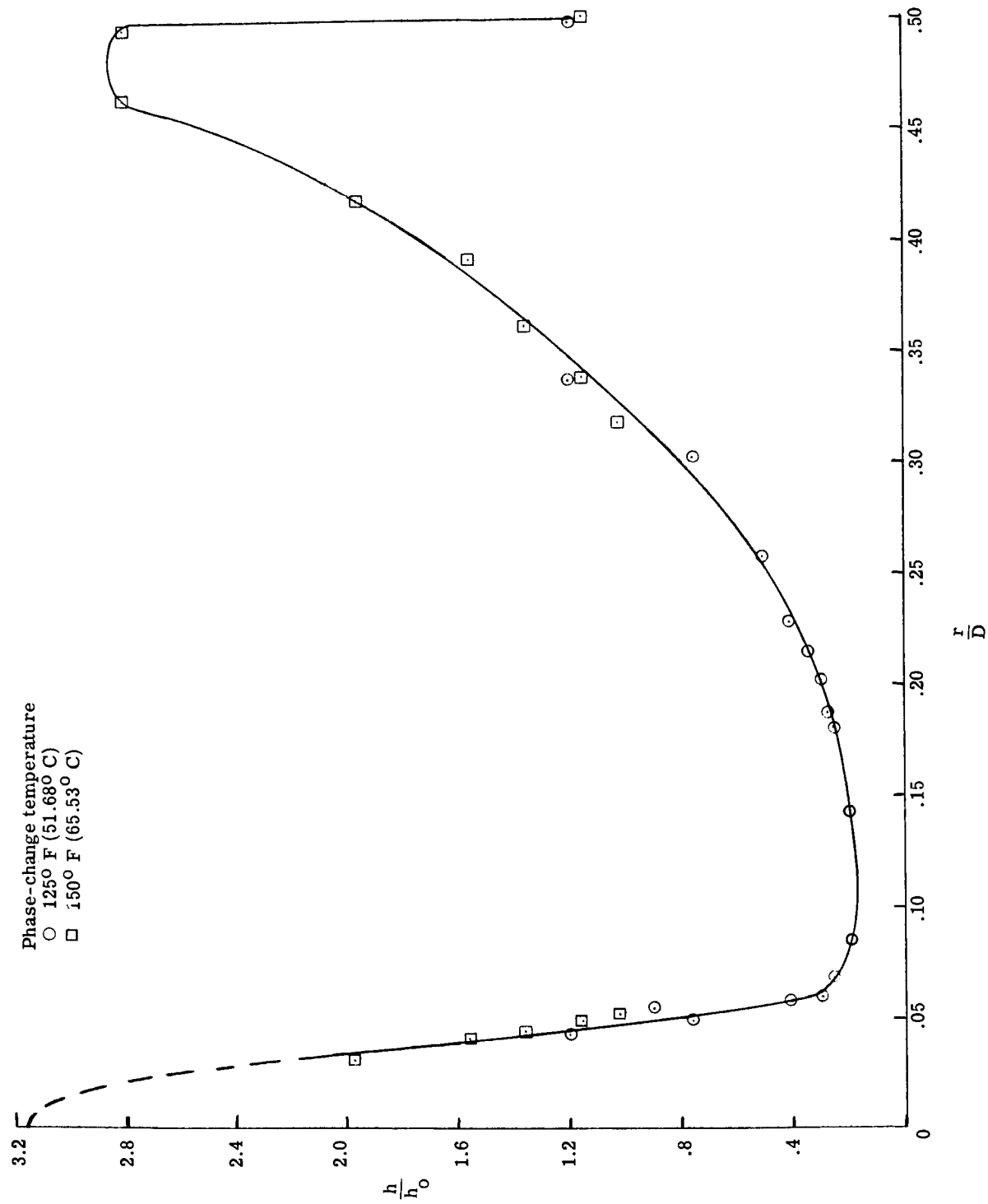
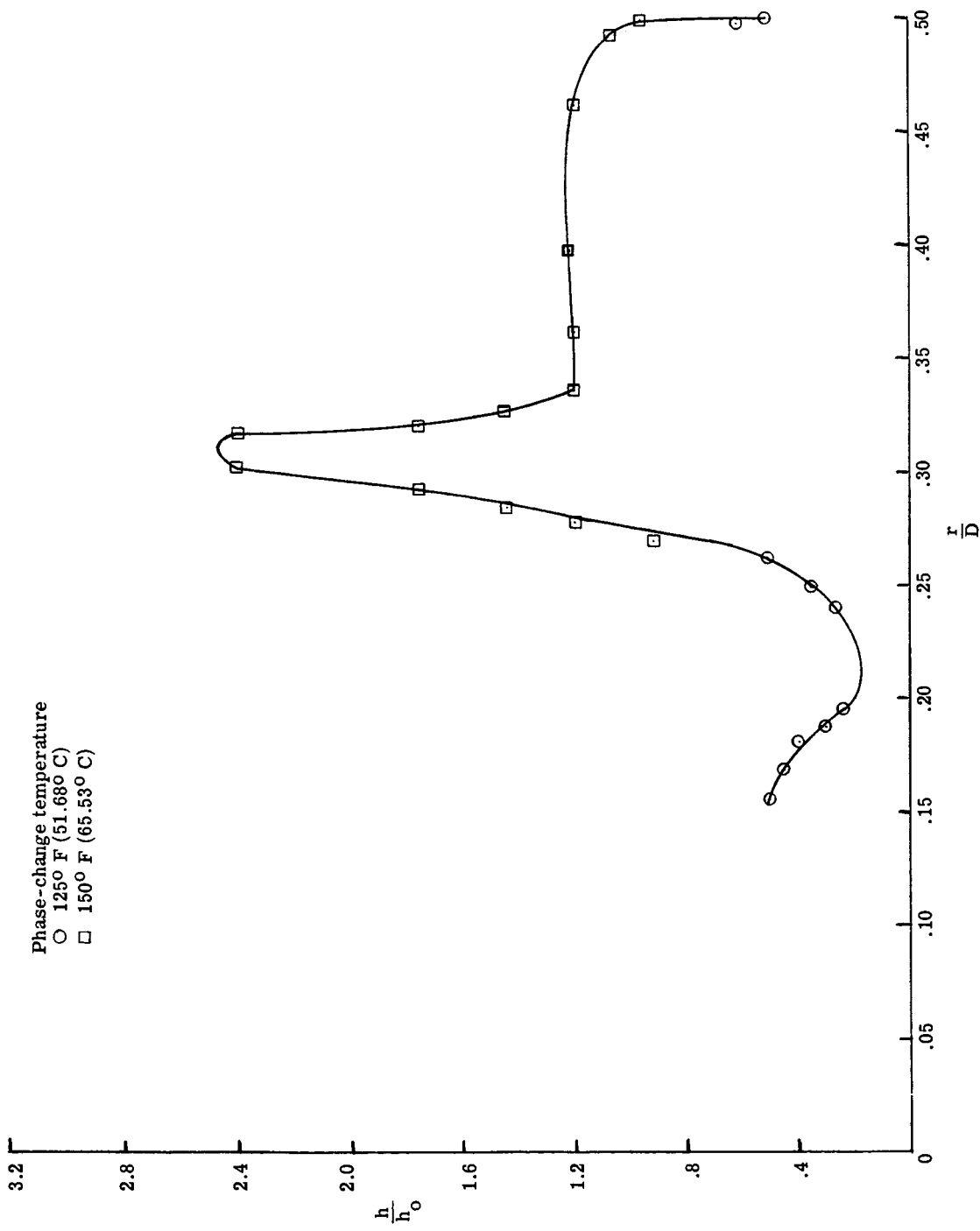


Figure 24.- Heat-transfer distribution for model 6 ( $r_n/D = 0.05$ ),  $\alpha = 0^\circ$ ;  $R_\infty D = 0.2 \times 10^6$ .





(a)  $\phi = 0^\circ$ .

Figure 25.- Heat-transfer distribution for model 5 ( $r_n/D = 0$ ).  $\alpha = 5^\circ$ ;  $R_{\infty, D} = 0.2 \times 10^6$ .

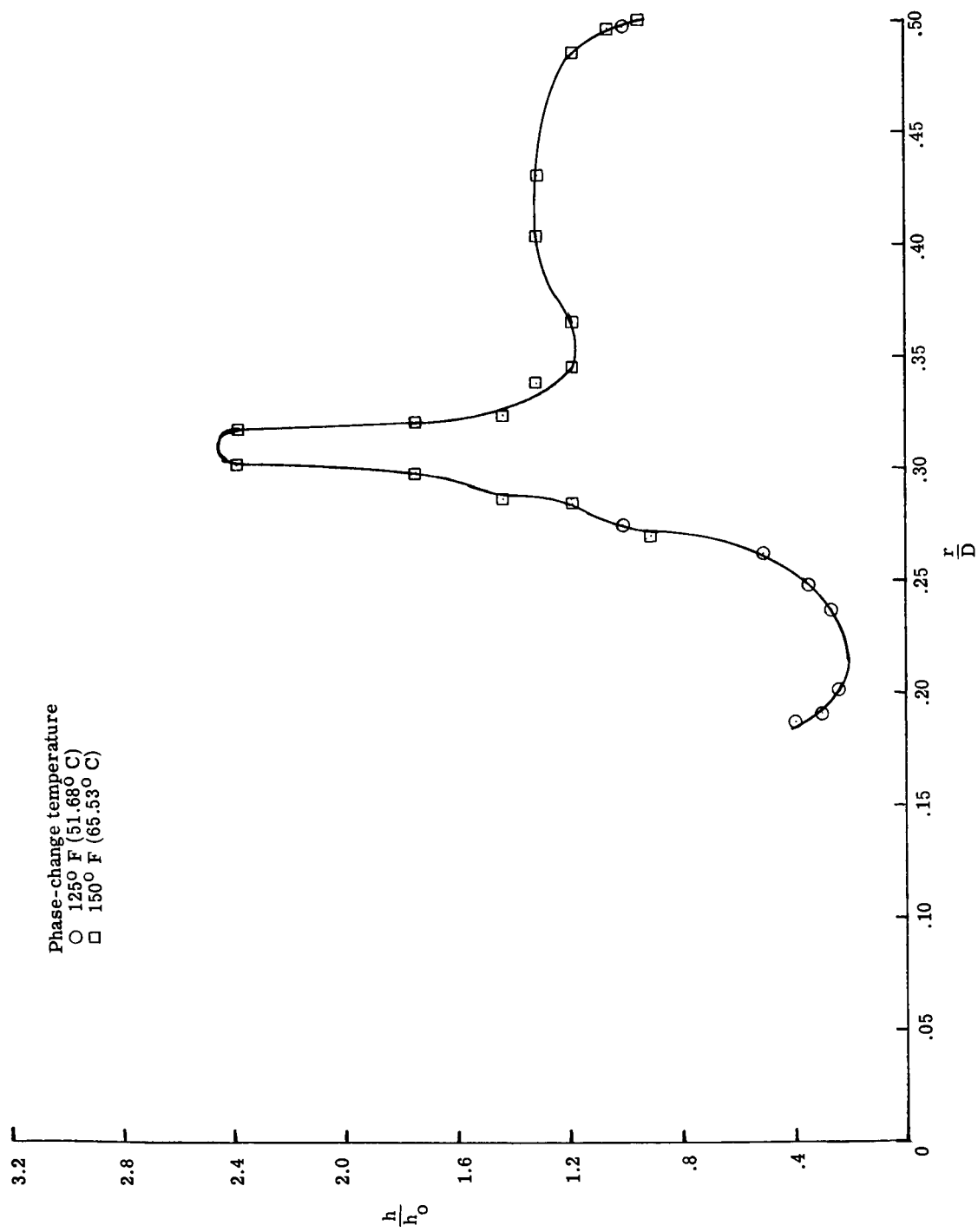
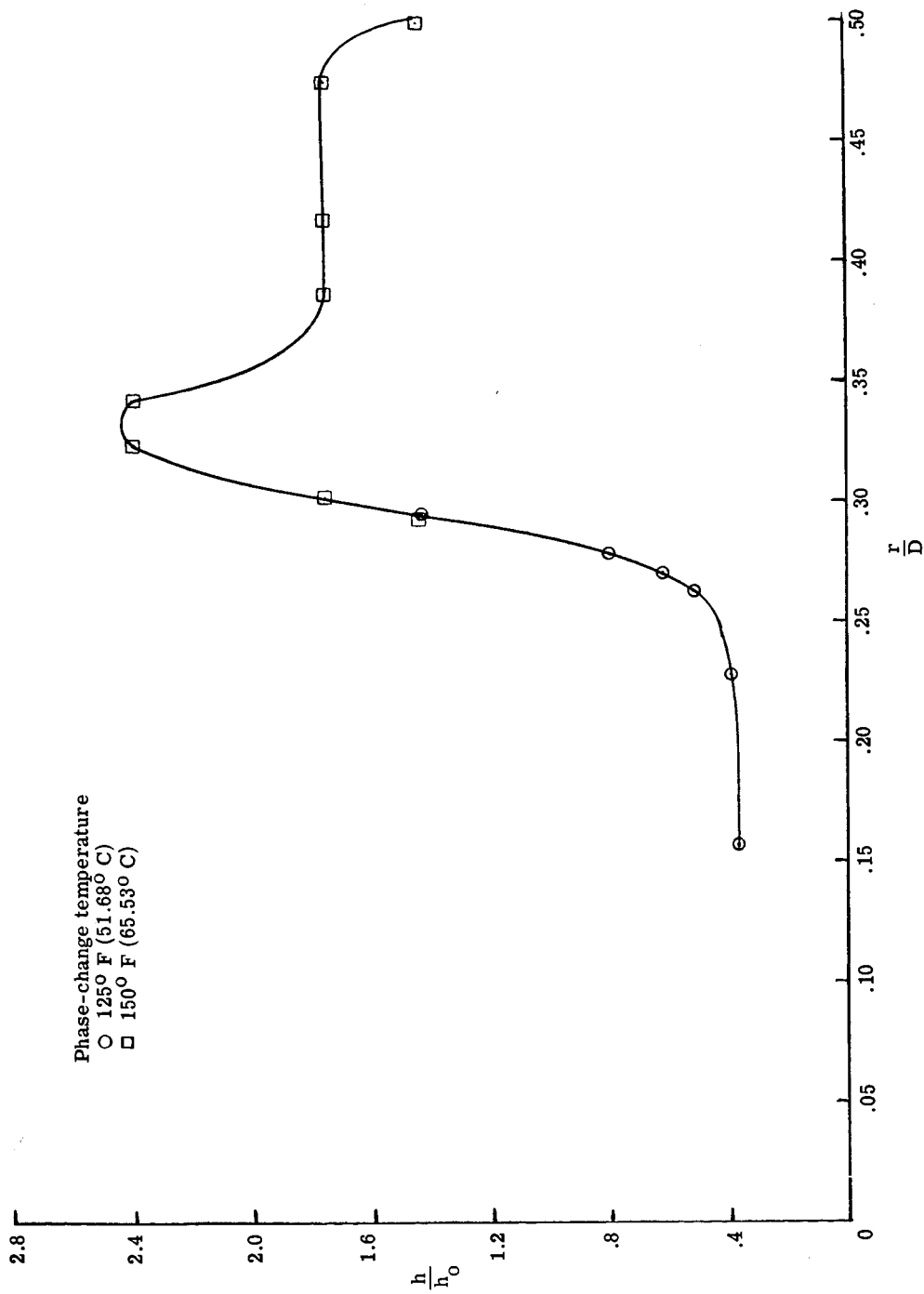
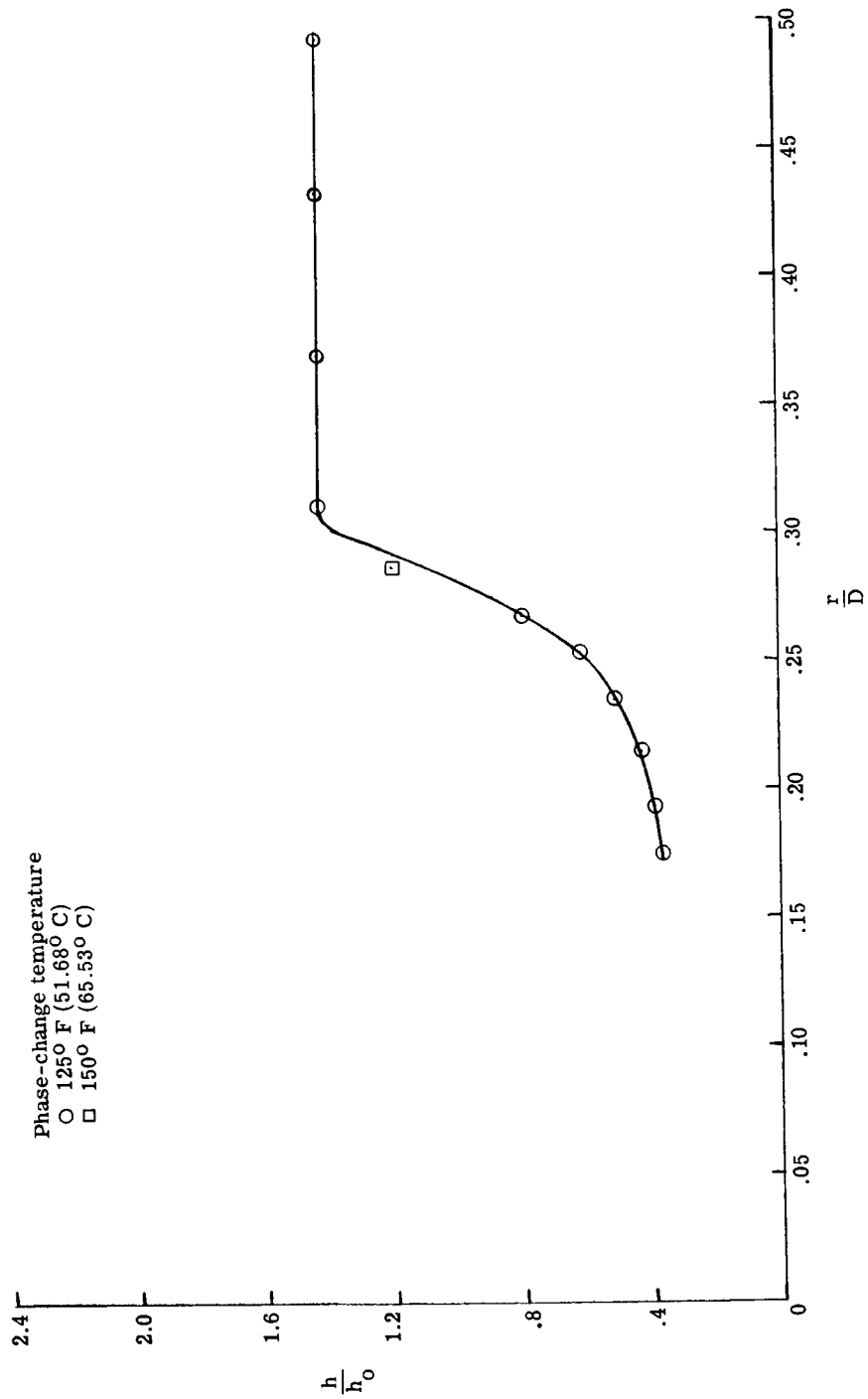
(b)  $\phi = 45^\circ$ .

Figure 25.- Continued.



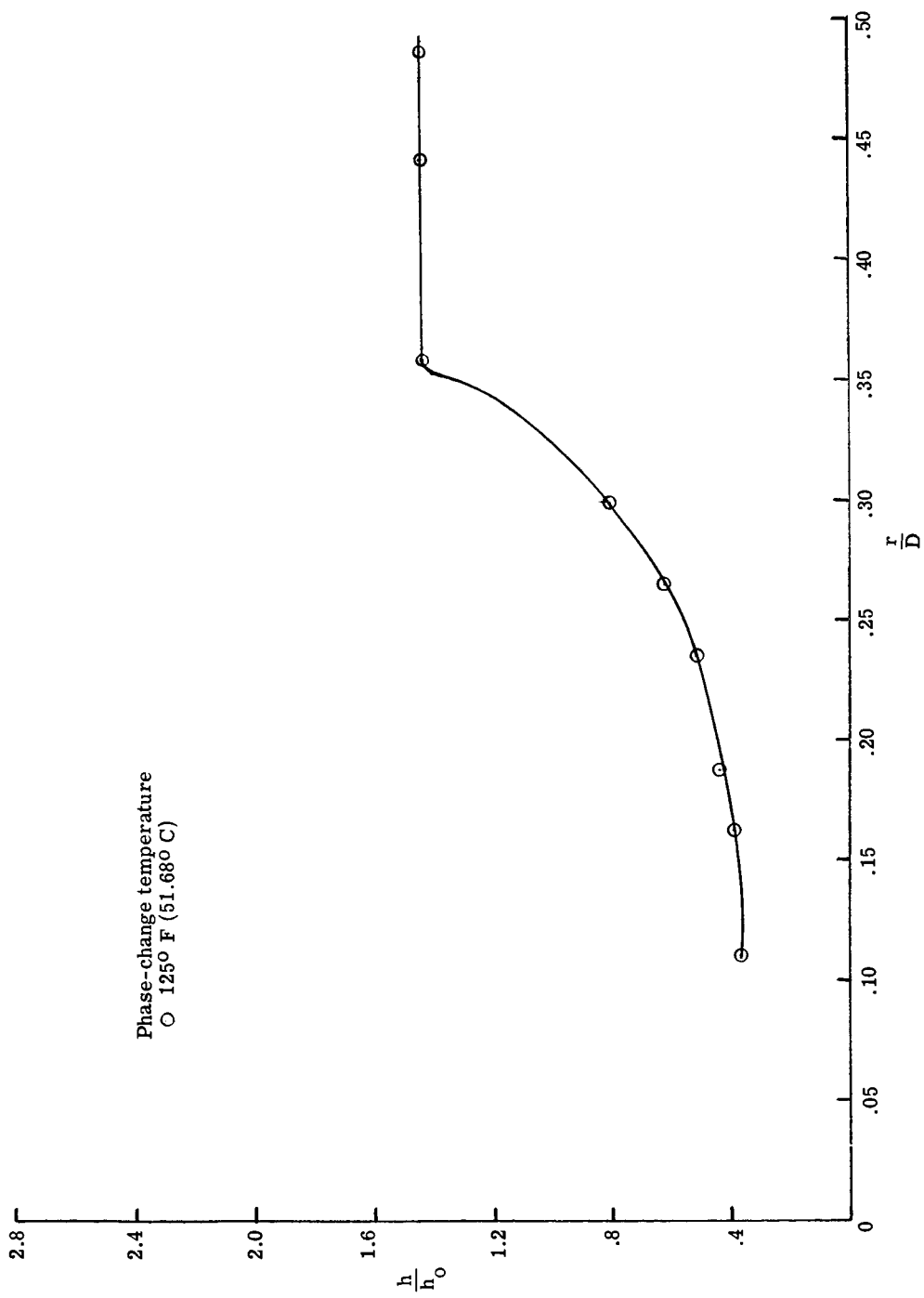
(c)  $\phi = 90^\circ$ .

Figure 25.- Continued.



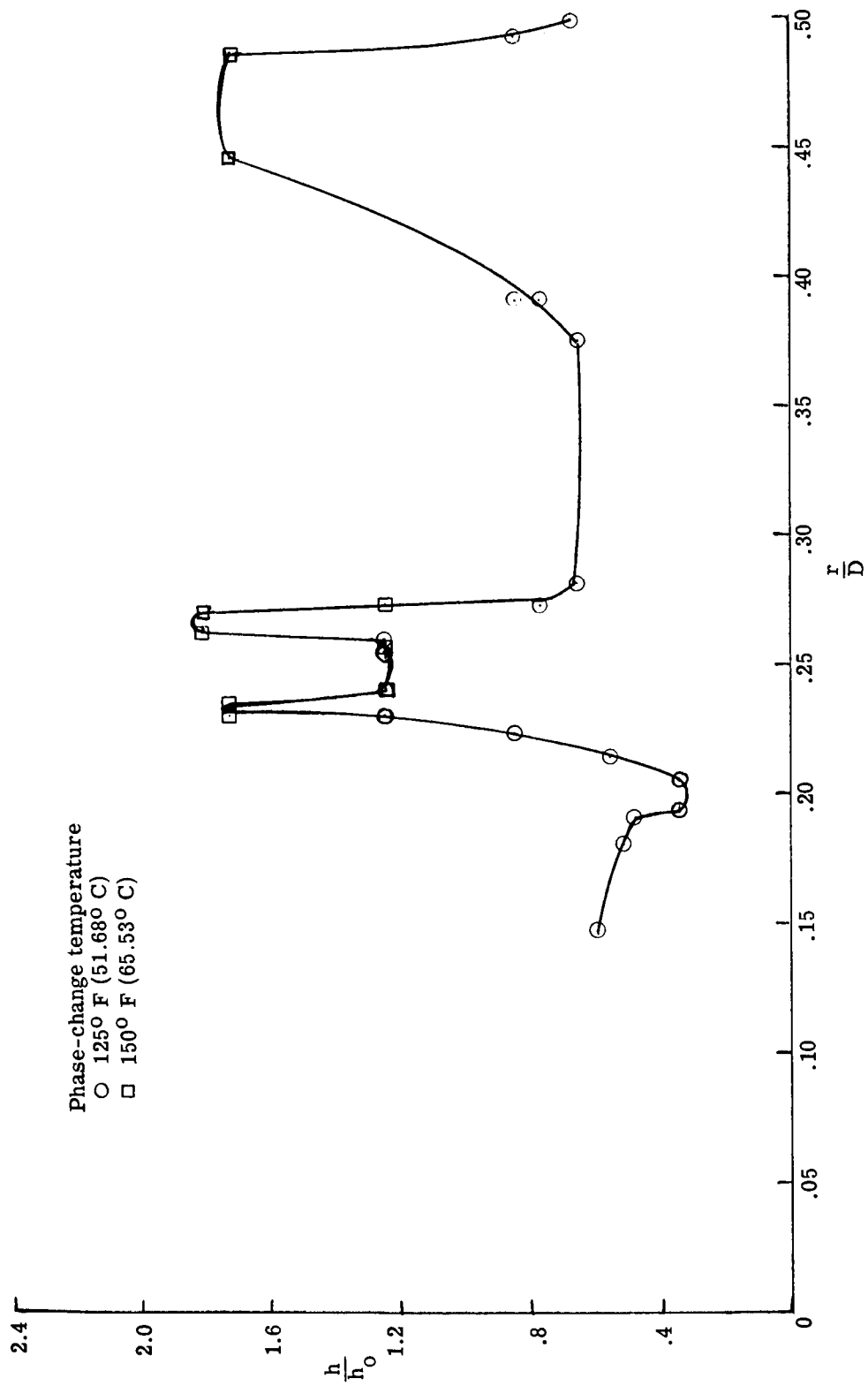
(d)  $\phi = 135^\circ$ .

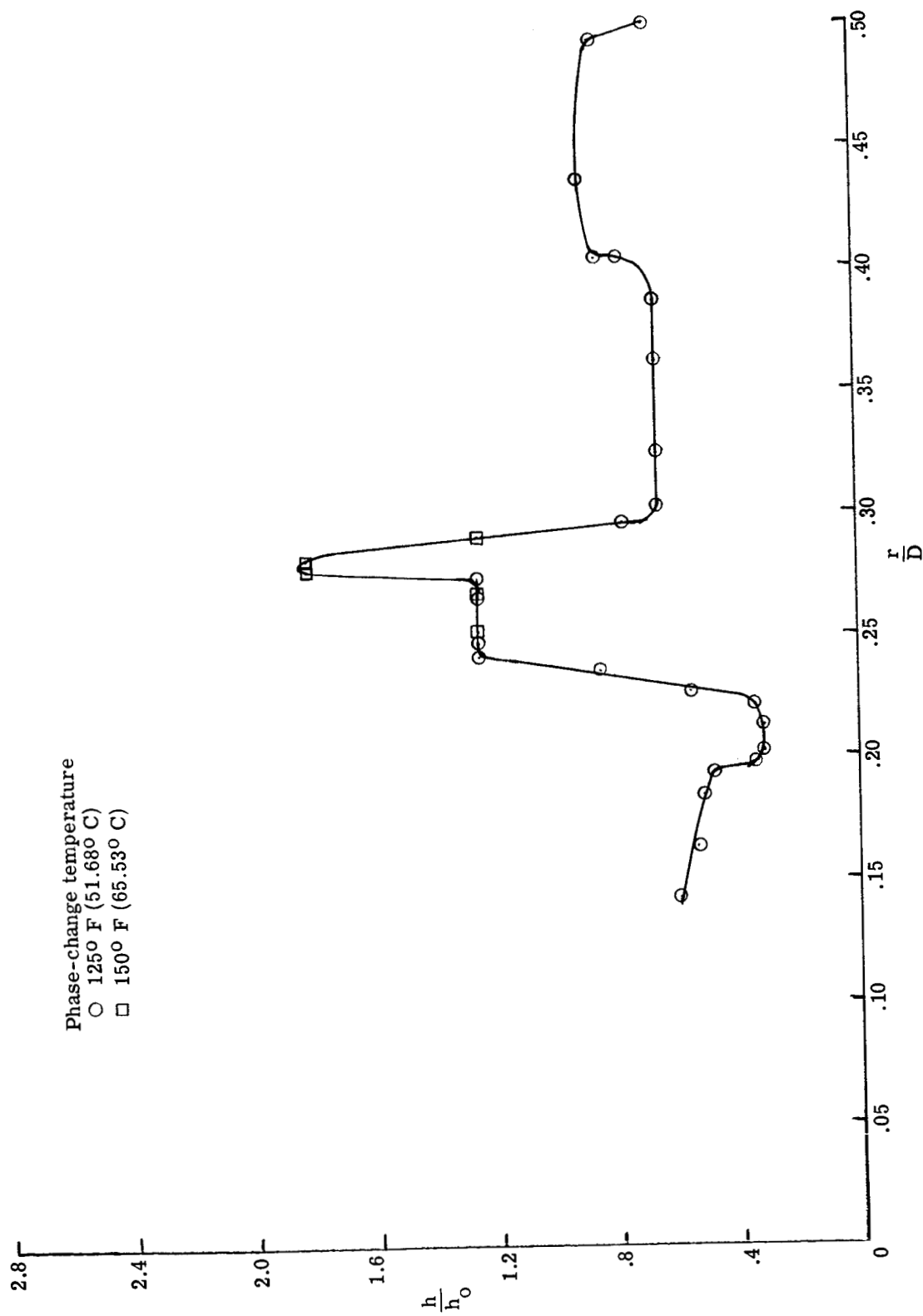
Figure 25.- Continued.



(e)  $\phi = 180^\circ$ .

Figure 25: - Concluded.

(a)  $\phi = 0^\circ$ .Figure 26.- Heat-transfer distribution for model 5 ( $r_n/d = 0$ ).  $\alpha = 12^\circ$ ;  $R_{\infty,D} = 0.2 \times 10^6$ .



(b)  $\phi = 45^\circ$ .

Figure 26.- Continued.

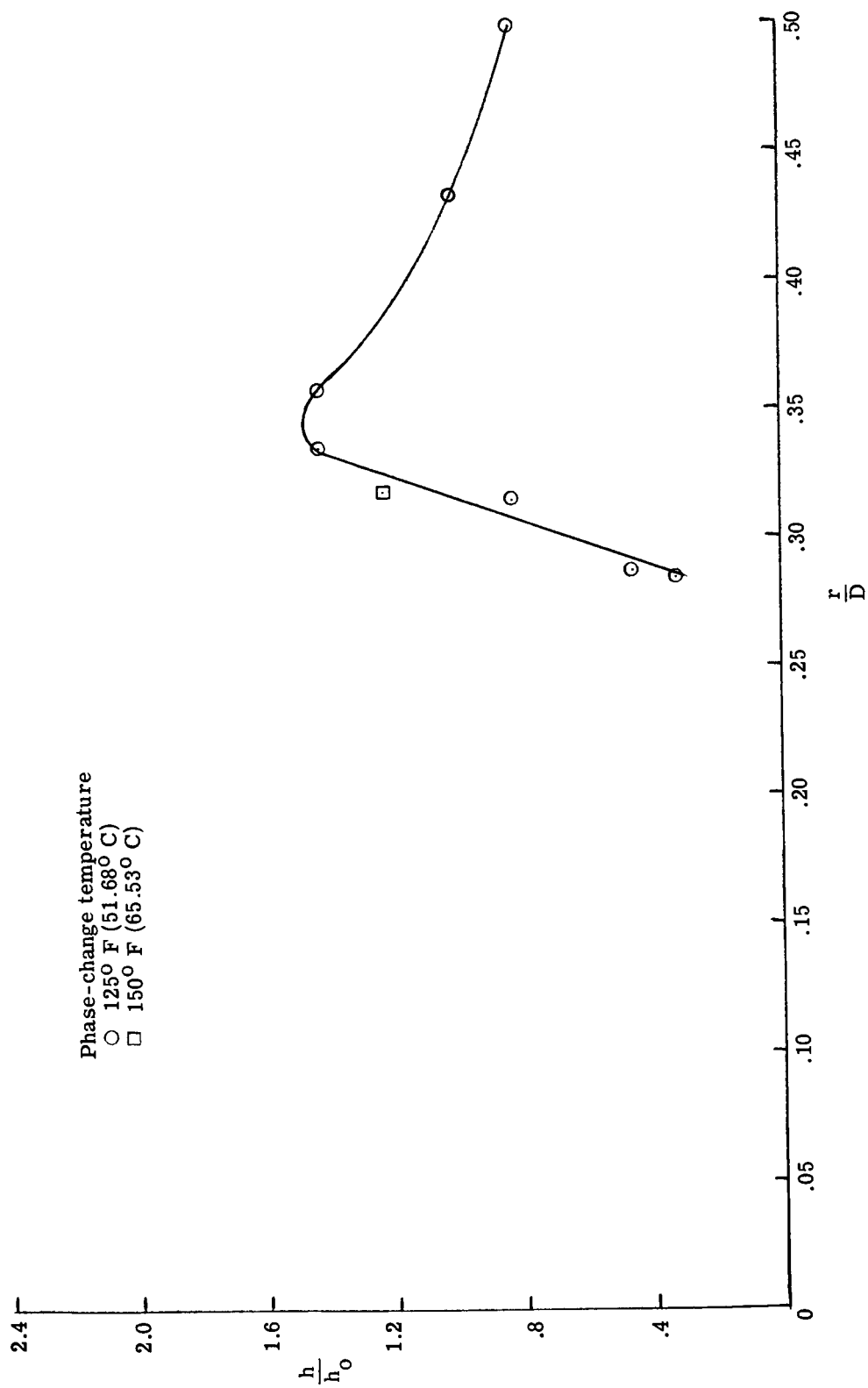
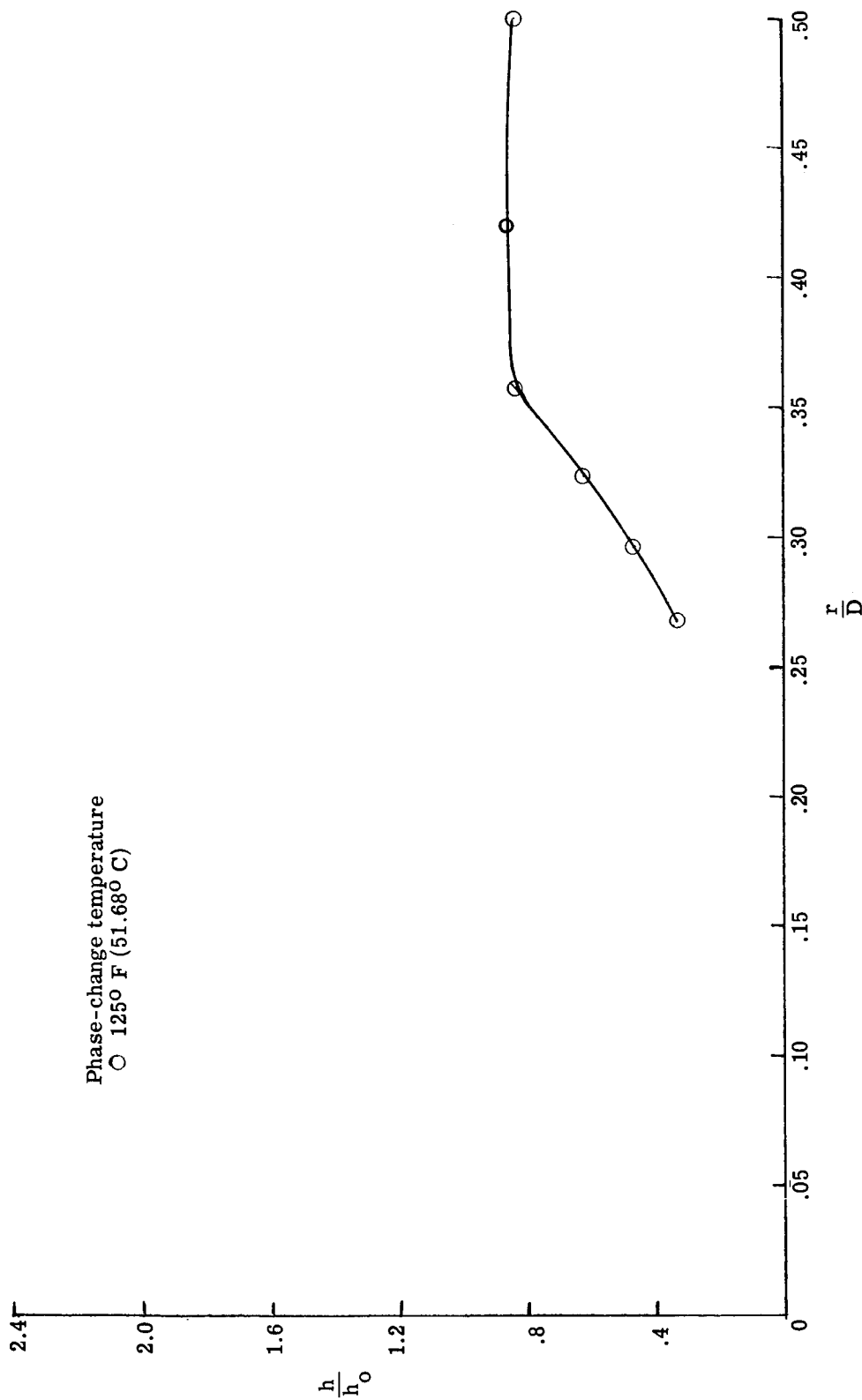
(c)  $\phi = 90^\circ$ .

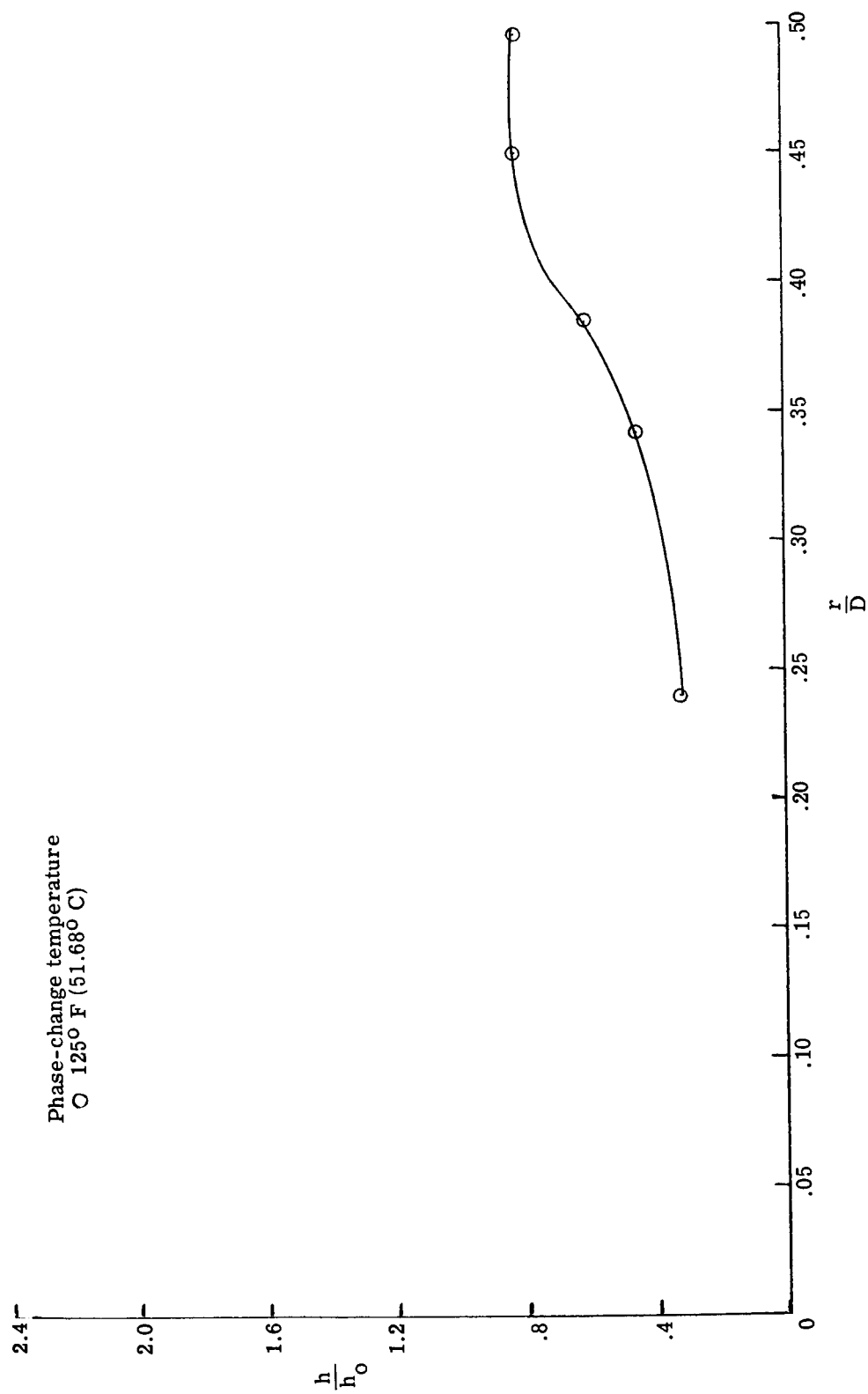
Figure 2a - Continued.





(d)  $\phi = 135^\circ$ .

Figure 26.- Continued.



(e)  $\phi = 180^\circ$ .

Figure 26.- Concluded.

01403  
188 up  
30-1-67

*"The aeronautical and space activities of the United States shall be conducted so as to contribute . . . to the expansion of human knowledge of phenomena in the atmosphere and space. The Administration shall provide for the widest practicable and appropriate dissemination of information concerning its activities and the results thereof."*

—NATIONAL AERONAUTICS AND SPACE ACT OF 1958

## NASA SCIENTIFIC AND TECHNICAL PUBLICATIONS

**TECHNICAL REPORTS:** Scientific and technical information considered important, complete, and a lasting contribution to existing knowledge.

**TECHNICAL NOTES:** Information less broad in scope but nevertheless of importance as a contribution to existing knowledge.

**TECHNICAL MEMORANDUMS:** Information receiving limited distribution because of preliminary data, security classification, or other reasons.

**CONTRACTOR REPORTS:** Technical information generated in connection with a NASA contract or grant and released under NASA auspices.

**TECHNICAL TRANSLATIONS:** Information published in a foreign language considered to merit NASA distribution in English.

**TECHNICAL REPRINTS:** Information derived from NASA activities and initially published in the form of journal articles.

**SPECIAL PUBLICATIONS:** Information derived from or of value to NASA activities but not necessarily reporting the results of individual NASA-programmed scientific efforts. Publications include conference proceedings, monographs, data compilations, handbooks, sourcebooks, and special bibliographies.

*Details on the availability of these publications may be obtained from:*

SCIENTIFIC AND TECHNICAL INFORMATION DIVISION  
NATIONAL AERONAUTICS AND SPACE ADMINISTRATION  
Washington, D.C. 20546